



3D hybrid coupled dual continuum and discrete fracture model for simulation of CO₂ injection into stimulated coal reservoirs with parallel implementation

Min Chen^{*}, Shakil A. Masum, Hywel R. Thomas

Geoenvironmental Research Centre, Cardiff School of Engineering, Cardiff University, CF24 3AA Cardiff, United Kingdom

ARTICLE INFO

Keywords:

Numerical modelling
Discrete fracture
CO₂ sequestration
THCM
Parallel computing

ABSTRACT

This work presents the development of a 3D hybrid coupled dual continuum and discrete fracture model for simulating coupled flow, reaction and deformation processes relevant to fractured reservoirs with multiscale fracture system, e.g., coal and shale, efficiently and accurately. In this hybrid model, the natural fracture network and coal matrix are described together by a dual continuum approach and the large fractures are represented explicitly by the discrete fracture approach. A combination of different types of elements is used for spatial discretization. Large fractures are discretised with lower-dimensional interface elements and continuum domains with higher-dimensional elements. The coupling between the two models is achieved via the principle of superposition. To reduce computational time of simulations for complex and large-scale problems, a hybrid MPI/OpenMP parallel scheme is implemented in this work. The developed model is applied to investigate coupled thermal, hydraulic, and mechanical processes associated with CO₂ sequestration and enhanced coalbed methane recovery. The results demonstrate capabilities of the model to adequately capture the effects of multiscale fracture system and their coupled behaviour during CO₂ injection and methane recovery from coal reservoirs. Performance of the proposed parallelisation scheme was tested by comparing computation times of serial and parallel implementations. A good performance improvement was achieved, the speedup using parallelized scheme reaches up to about 10 times along with satisfactory scalability for considered application example. The findings of this work support developments and improvements of efficient advanced numerical models to study coupled THCM behaviour in fractured porous geomaterials.

1. Introduction

Numerical modelling techniques are often implemented in understanding large spatio-temporal subsurface flow, reaction, and deformation problems encountered in geoenvironmental and geo-energy applications, such as carbon sequestration, nuclear waste disposal, contaminated land remediation, oil and gas recovery, geothermal energy etc. (Chen et al., 2019; Cui et al., 2022; Rutqvist et al., 2002; Taron et al., 2009). These techniques involve approximation of governing partial differential equations and finding approximate solutions that are close to the exact solutions of a specific problem. Numerous methods have been developed over the years. An overview of the popular computational methods has been presented in Jing (2003), Lei et al. (2017) and Jenabidehkordi (2019). However, for subsurface flow and deformation problems, finite element and/ finite volume methods for

spatial discretisation and finite difference methods for temporal discretisation are often implemented or preferred. Although the methods are well established, understood and widely applied, they still suffer from computational efficiency, especially for complex and coupled problems. For example, numerical modelling of carbon sequestration or coalbed methane recovery involves multi-scale, multi-phase flow and mass transfer processes occurring at multiple interconnected model domains. Numerical simulations of such problems are computationally demanding and require implementation of high-performance computational platforms for adequately capturing the processes occurring at all scales in model simulations (Thomas et al., 2010).

Coalbeds are highly fractured media containing porous matrices, cleat network, and large scale geological fractures like faults. The modelling concepts for fractured porous media are usually based on equivalent continuum model (EC), multi-continuum model (MC),

^{*} Corresponding author.

E-mail address: Chenm24@cardiff.ac.uk (M. Chen).

<https://doi.org/10.1016/j.coal.2022.104103>

Received 3 March 2022; Received in revised form 6 July 2022; Accepted 14 September 2022

Available online 22 September 2022

0166-5162/© 2022 The Authors. Published by Elsevier B.V. This is an open access article under the CC BY license (<http://creativecommons.org/licenses/by/4.0/>).

discrete fracture-matrix model (DFM) and discrete fracture network model (DFN). Among these, the MC approach proposed by Barenblatt et al. (1960), has been widely improved and applied to predict flow and transport in fractured rocks, because of its advantages in representation accuracy, computational efficiency and field practicality. In their approach, Barenblatt et al. (1960) represented a fractured porous medium as two or more overlapping continua. Dual continuum models, also known as dual porosity model (DP), are the most common form of multi-continuum model (e.g. Chen et al., 2019; Gerke and Genuchten, 1993; Hosking et al., 2017; Masum et al., 2022). This approach can capture different characteristics of fractures and rock matrices in a systematic way. The fracture continuum generally covers the conductive part, whereas the matrix continuum generally provides the storage capacity. For reservoirs of highly connected small-scale fractures, conventional DP model offers a better representation of flow characteristics, but this modelling approach fails to accurately represent large-scale fractures like hydraulic fracture and localized anisotropy. The DFM model overcomes the limitations of the dual-continuum approach by representing individual large-scale fractures explicitly (Moinfar et al., 2013). The combination of DP model and DFM model perhaps provide a promising approach to account for the effects of multiscale fracture systems. However, when such hybrid model is used, especially for 3D problems, additional treatments are required for improvement of computational efficiency. For example, simulation domain can be reduced geometrically from a higher dimension to a lower dimension or by applying principle of symmetry (Chen et al., 2019, 2020a). When high spatial resolution results are not required, coarsely discretised mesh can be considered. However, many cases are inherently three-dimensional due to the geometry of the analysed domain, as well as circumstances where accuracy of results requires the whole system to be considered during model simulations (Vardon et al., 2011). Development of more efficient numerical algorithms and faster solution schemes are therefore essential to reduce computational time.

With increasing computing power, high performance computing (HPC) is becoming a desired technique to process data and perform complex calculations at faster speeds (Kolditz et al., 2006; Thomas et al., 2010; Vardon et al., 2009). Parallel processing technique, which involves multiple, connected computers via fast communication networks or computers with multiple processors (dual-core, quad-core, super-computers, etc), is the most commonly used approach to speed-up finite element or finite volume methods together with subsurface coupled flow and deformation models (Chiang and Fulton, 1990; Smith et al., 2013). Domain decomposition method where sections of a domain are solved independently, is often used in parallel computational method. Jimack and Touheed (2000) discussed the details of a simple parallel finite element algorithm based on domain decomposition method. Similar parallel finite element scheme has also been developed by Wang et al. (2009) for multi-physical processes in porous media. But more care is required when splitting a domain in terms of limiting iterations for convergence and computational work-balancing. For the sake of efficiency, third-party Mesh-partitioning Tools METIS (Karypis and Kumar, 1999) has been used to split finite element mesh prior to the calculation and the Portable Extensible Toolkit for Scientific Computation (PETSc) has been used for solution (Wang et al., 2017). However, these tools should be integrated into existing codes which cannot be achieved easily in most cases (Castro et al., 2009).

The motivation of this work is driven by the necessity for improving computational efficiency while maintain adequate accuracy of a coupled finite element based model for CO₂ storage in fractured reservoirs like coalbeds and shale. In this paper, the previously developed model of (Chen et al., 2020b) is extended using a parallel, finite element based scheme to model coupled THCM problems for large-scale, three-dimensional applications. This paper includes (1) the development of a theoretical model for non-isothermal, multicomponent flow through elastically deformable unsaturated fractured rock under a coupled thermal, hydraulic, chemical, and mechanical framework, (2) a hybrid

coupled dual continuum and discrete fracture model accounting the effects of multiscale fractures, in which numerous small scale fractures network and porous matrix are modelled with dual continuum model and the large scale fractures are represented explicitly using discrete fracture model, and (3) a hybrid Message Passing Interface (MPI)/Open Multi-Processing (OpenMP) method to parallelise the computer code. The structure of this paper is as follows: firstly, a comprehensive theoretical framework for modelling coupled processes in fractured porous geomaterials based on hybrid coupled dual continuum and discrete fracture model is presented along with numerical solution in section 2. Section 3 presents the details on hybrid MPI/OPENMP parallelization scheme, followed by verification and validation tests in section 4. An application example in CO₂-enhanced coalbed methane recovery is presented in section 5. Analyses and discussion of the computational efficiency of the proposed parallel scheme is presented in detail in Section 6. Finally, the conclusions are drawn in section 7.

2. Model development

Coal reservoirs are highly heterogeneous systems of multi-scale fractures including a uniformly distributed network of natural fractures i.e., cleats, and sparse, large-scale fractures such as faults, hydraulic fractures etc., as shown Fig. 1(a). It is not feasible to represent numerous pre-existing fractures individually and explicitly. Due to conductivity contrast and roles of fracture scales, only the large fractures are modelled explicitly with discrete fracture model. The coal cleat network and coal matrix are modelled using a dual continuum approach. Fig. 1(b) shows flow connectivity between dual continuum and discrete fracture models. The proposed model consists of three different media: (i) matrix continuum with relatively large porosity and low permeability, (ii) fracture continuum with intermediate porosity and permeability, and (iii) discrete fractures with relatively high permeability. Mass exchange may take place between any two pore regions. However, the fluid in the larger fractures has a preference to penetrate into the natural fractures network due to much higher permeation of fracture network compared to rock matrices. Hence, in this work, mass exchange between matrix continuum and hydraulic fractures is neglected because the matrix continuum predominantly exchanges mass with the natural fracture network. Fig. 1(b) illustrates the flow connectivity between different continua.

Theoretical formulations describing non-isothermal, multiphase, multicomponent gas flow in deformable coalbeds are presented below. Following assumptions are made: (1) The cleat network and matrix regions of coals are treated as homogenous and isotropic continua. (2) Each continuum is treated as a multiphase system of solid, liquid, and gas. Hence, voids are filled partially with liquid water and partially with gas. (3) Coalbeds are in local thermal non-equilibrium (LTNE). (4) Coal deformation is linear and elastic. In the following sections, fracture and matrix continua are denoted by subscripts $\kappa = f, m$. Pore regions, e.g., fracture continuum, matrix continuum, and discrete fractures are denoted by subscripts $\alpha = f, m, F$, respectively; and solid and fluid phases (gas and water) are denoted by subscripts $\beta = s, l$, respectively. Gas species in a multi-component system is labelled by superscripts $i = 1, 2, 3, \dots, n_g$. Detailed descriptions and derivations of the equations are available in (Chen, 2019).

2.1. Mass balance equation

Based on the principle of conservation of mass, the governing equations for water flow can be expressed as:

$$\frac{\partial}{\partial t}(S_{ik}\rho_i n_\kappa) = -\nabla \cdot (\rho_l \mathbf{v}_{ik}) + \Gamma_{ik} \kappa = [f, m] \quad (1)$$

And multicomponent reactive gas flow can be expressed as:

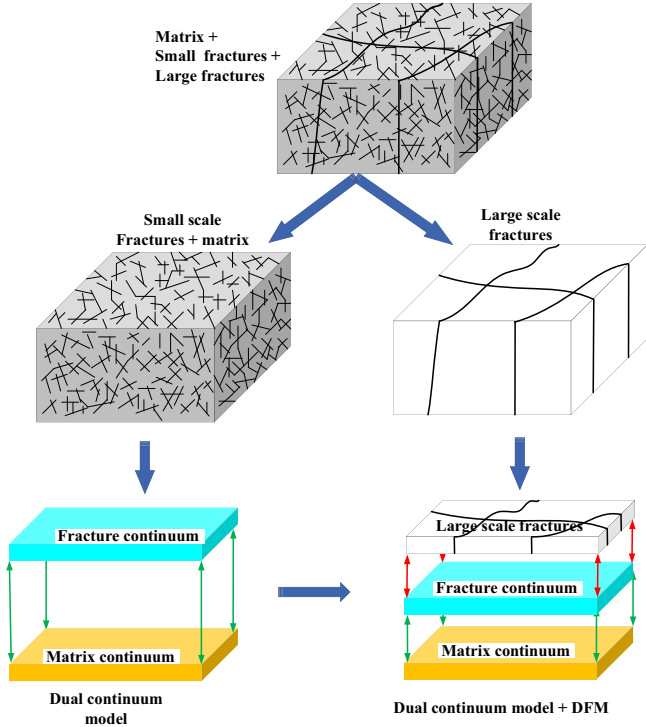


Fig. 1. (a) Conceptual development process for the hybrid dual continuum and discrete fracture model. (b) Flow connectivity between multiple pore regions in the proposed model (W: injection well, LF: large scale fractures, SF: Fracture continuum, and MC: matrix continuum).

$$\frac{\partial}{\partial t} (c_{gk}^i S_{gk} n_k + c_{dk}^i S_{lk} n_k) = \nabla \cdot \mathbf{q}_{gk}^i + \nabla \cdot \mathbf{q}_{dk}^i + R_{gk}^i + \Gamma_{gk}^i \quad (2)$$

As mentioned above, the discrete fracture model is used to represent the large fractures explicitly. Because of high aspect ratio of large fracture with thickness orders of magnitude lower than its length, the large scale fracture is treated as a lower dimensional object, that is, 2D plane in 3D space, as shown in Fig. 2. Therefore, the flow continuity of fluid in large fractures can be written as:

$$\frac{\partial}{\partial t} (w \rho_l S_{lF}) = -w \nabla_l \cdot (\rho_l \mathbf{v}_{lF}) + \Gamma_{lF} \quad (3)$$

$$\frac{\partial}{\partial t} (c_{gF}^i S_{gFW} + c_{dF}^i S_{lFW}) = -\nabla_{ld} \cdot \mathbf{q}_{gF}^i - \nabla_l \cdot \mathbf{q}_{dF}^i + \Gamma_{gF}^i + R_{gF}^i \quad (4)$$

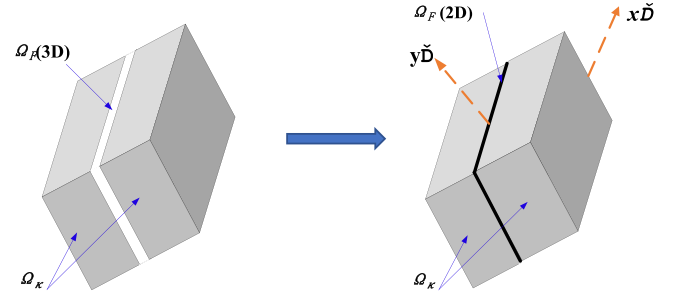


Fig. 2. Schematic representation of the discrete fracture matrix approach (x' - y' is local coordinate).

where n_k is porosity, $\kappa = f, m$, $S_{l\alpha}$ is degree of water saturation, $\alpha = f, m, F$, $S_{g\alpha}$ is the degrees of gas saturation, ρ_l is the density of water, $\mathbf{v}_{l\alpha}$ is the water velocity, $c_{g\alpha}^i$ is gas concentration in gas phase, $c_{d\alpha}^i$ is the concentration of the gas dissolved in the water phase, $\mathbf{q}_{g\alpha}^i$ and $\mathbf{q}_{d\alpha}^i$ are the fluxes of the i^{th} gas component in the gas phase and in the liquid phase, $\Gamma_{l\alpha}$ and $\Gamma_{g\alpha}^i$ sink-source term for mass exchange between different pore regions, and $R_{g\alpha}^i$ represents the sink-source term for geochemical reactions. w is the fracture aperture, ∇_l is the lower dimensional gradient operator, for example, if $\nabla = \frac{\partial}{\partial x} + \frac{\partial}{\partial y} + \frac{\partial}{\partial z}$, ∇_{ld} can be expressed as $\nabla_{ld} = \frac{\partial}{\partial x'} + \frac{\partial}{\partial y'}$, \mathbf{x}' - \mathbf{y}' is local coordinate, as shown in Fig. 2.

Assuming a thermodynamic equilibrium between the dissolved gas and the free gas, concentration of the dissolved gas in eqs. (2) and (4) can be obtained with Henry's law (Kühne et al., 2005):

$$c_{d\alpha}^i = H_g^i(T) p_{g\alpha}^i \quad (5)$$

where H_g^i is the Henry's coefficient to determine dissolved gas volume in water, $p_{g\alpha}^i$ is partial pressure of i^{th} species.

Gas flow is generally considered to be driven by advection and diffusion, and the fluxes $\mathbf{q}_{g\alpha}^i$ and $\mathbf{q}_{d\alpha}^i$ can be given as:

$$\mathbf{q}_{g\alpha}^i = c_{g\alpha}^i \mathbf{v}_{g\alpha} - S_{g\alpha} D_{g\alpha} \nabla c_{g\alpha}^i \quad (6)$$

$$\mathbf{q}_{d\alpha}^i = c_{d\alpha}^i \mathbf{v}_{l\alpha} - S_{l\alpha} D_{d\alpha} \nabla c_{d\alpha}^i \quad (7)$$

where $\mathbf{v}_{g\alpha}$ is the velocity of the gas phase and $D_{d\alpha}$ is effective diffusion coefficient.

Following Darcy's law, velocity of fluids is expressed as:

$$\mathbf{v}_{\beta\alpha} = -\frac{K_\alpha K_{r\beta\alpha} \nabla p_{\beta\alpha}}{\mu_{\beta\alpha}} \quad (8)$$

where K_α is the intrinsic permeability. For hydraulic fractures, the permeability is associated with fracture aperture, which can be calculated by $K_F = w^2/12$ (Pouya, 2015). The variations of permeability is stress dependent, $K_k = K_{k0} \exp(-C_{pk} \Delta \bar{\sigma})$, K_{k0} is permeability at reference state, C_{pk} is pore compressibility and it is influenced by stress state and coal-gas interaction (Chen et al., 2022), and $\bar{\sigma}$ is mean stress, $K_{r\beta\alpha}$ is the relative permeability to water ($\beta = l$) or gases ($\beta = g$), $\mu_{\beta\alpha}$ is the fluid viscosity. The gas mixture viscosity is calculated using method of Chung et al. (1988) in this work, $p_{\beta\alpha}$ is fluid pressure. For real gases, the gas pressure is expressed as:

$$p_{g\alpha} = Z_\alpha R T_\alpha \sum_{i=1}^{n_g} c_{g\alpha}^i \quad (9)$$

where T_α is temperature, and Z_α is gas compressibility factor, which is calculated with the Peng-Robinson equations of state or PR-EoS (Peng and Robinson, 1976).

The relative permeability to water is associated with the degree of saturation and calculated following the van Genuchten model (Van

Genuchten, 1980):

$$K_{rta} = S_{lae}^{1/2} [1 - (1 - S_{lae}^{1/\psi_\alpha})^{\psi_\alpha}]^2 \quad (10)$$

where S_{lae} is the effective water saturation and it is calculated using the following capillary pressure-saturation relationship (Van Genuchten, 1980):

$$S_{lae} = \frac{S_{la} - S_{lar}}{S_{lmax} - S_{lar}} = \left(1 + \left|\frac{S_{la}}{p_{0\alpha}}\right|^{\gamma_\alpha}\right)^{-\psi_\alpha} \quad (11)$$

where S_{lmax} is the maximum water saturation, S_{lar} are the residual water saturation, γ_α and ψ_α ($\psi_\alpha = 1 - 1/\gamma_\alpha$) are constants based on the water retention characteristics and $p_{0\alpha}$ is a characteristic pressure, $p_{0\alpha}$ are different for fractures and porous matrix.

Bogdanov et al. (2003) proposed a simple model for gas phase relative permeability in fractures:

$$K_{rgf} = (1 - S_{lf})^N \quad (12)$$

where N is the power exponent for the relative permeability in fractures, such relative permeability relationship is also used for large fractures.

Gas sorption in coal mainly occurs at the surfaces of coal matrices. Therefore, $R_{gf}^i = 0$, $R_{gf}^i = 0$. The sink/source of or the i^{th} gas component from gas adsorption in matrix pores is expressed as:

$$R_{gm}^i = -\frac{dR_{gm \rightarrow ad}^i}{dt} \quad (13)$$

$$R_{gm \rightarrow ad}^i = \rho_s c_s^i \quad (14)$$

where c_s^i is adsorbed gas concentration, ρ_s is coal density.

Adsorption of multicomponent gases in coal is generally described with extended Langmuir isotherm model:

$$c_s^i = \frac{c_L^i b_L^i x_{gm}^i p_{gm}}{\sum_{i=1}^n b_L^i x_{gm}^i p_{gm} + 1} \quad (15)$$

where x_{gm}^i is molar gas fraction of the i^{th} species, c_L^i is the Langmuir volume constant, and b_L^i is the Langmuir pressure constant, which are affected by temperature and moisture content, given as (Chen et al., 2020c, 2021):

$$c_L^i = c_{L0}^i \exp(-\delta^i \Delta T_\alpha - \xi^i m_w) \quad (16)$$

$$b_L^i = b_{L\infty}^i \exp\left(\frac{E_{in}^i}{RT}\right) \quad (17)$$

$$m_w = \frac{\rho_l n_m S_{lm}}{\rho_s} \quad (18)$$

where c_{L0}^i is the theoretical maximum adsorption capacity for gases, δ^i is a reduction coefficient related with temperature increase, ξ^i is an adsorption capacity decay coefficient with moisture content (m_w) in weight percentage before equilibrium moisture content, E_{in}^i is the interaction energy between the adsorbate and the adsorbent, and $b_{L\infty}^i$ is the affinity at infinite temperature.

In addition to the sink-source from gas adsorption expressed in eq. (13), the mass exchange between different regions can also contribute to the sink-source term. Water flow between fracture and matrix continua are estimated by the mass exchange term, Γ_{la} . It has been suggested that a quasi-steady state water pressure distribution prevails in coal matrix blocks. The process is purely advective, and the water exchange rate is expressed as a linear function of the difference between the average pore water pressures in the fracture and the matrix continua (Barenblatt et al., 1960; Warren and Root, 1963):

$$\Gamma_{lf} = -\Gamma_{lm} = -\sigma_l (p_{lf} - p_{lm}) \quad (19)$$

where σ_l is the mass exchange coefficient for water.

The mass exchange between both continua includes the exchange in gas phase and also in liquid phase as dissolved state. It is expressed as:

$$\Gamma_{gf} = -\Gamma_{gm} = -\sigma_{gD} (c_f^i - c_m^i) - \bar{c}_d \sigma_l (p_{lf} - p_{lm}) \quad (20)$$

Where \bar{c}_d is the average dissolved gas concentration between both continua. σ_{gD} is the first order mass exchange coefficient for diffusion of the i^{th} gas component, which is given by:

$$\sigma_{gD} = \frac{a}{l_b^2} D_{gem}^i \quad (21)$$

where a is a factor related to geometry of the matrix blocks, $a = 3\pi^2$ for 3D cases, D_{gem}^i is effective diffusion coefficient of the i^{th} gas component and l_b is the matrix block length.

2.2. Energy balance equation

In this study, a local thermal non-equilibrium (LTNE) approach is applied to consider heat transfer between different domains. However, there is no heat exchange between the phases in individual continuum, in other words, different phases always have the same temperature in a single continuum. The energy balance question can be expressed as (Hosking et al., 2020):

$$(\rho_k C_{pk})_{eff} \frac{\partial T_k}{\partial t} = \nabla \cdot (\lambda_{ek} \nabla T_k) - (S_{lk} \rho_l C_{pl} \mathbf{v}_{lk} + S_{gk} \rho_{gk} C_{pgk} \mathbf{v}_{gk}) \cdot \nabla T_k + q_k \quad (22)$$

For heat transfer through the fluid in the discrete fractures can be written as:

$$w(\rho_f C_{pf})_{eff} \frac{\partial T_f}{\partial t} = \nabla \cdot (w \lambda_{ef} \nabla T_f) - (w S_{lf} \rho_l C_{pl} \mathbf{v}_{lf} + w S_{gf} \rho_{gf} C_{pgf} \mathbf{v}_{gf}) \cdot \nabla T_f + q_f \quad (23)$$

where $(\rho_k C_{pk})_{eff}$ and λ_{ek} are effective specific heat capacity and effective the average thermal conductivity of each continuum, q_k is heat source accounting for heat transfer among pore domains and heat supply, for example, through geochemical reactions.

Effective specific heat capacity can be obtained from the density and specific heat capacities of all components within a coal matrix as (Gupta et al., 2015):

$$(\rho_m C_{pm})_{eff} = (1 - n_m - n_f) (\rho_s C_{ps} + \rho_a C_{pa}) + n_m S_{lm} \rho_l C_{pl} + n_m S_{gm} \rho_{gm} C_{pgm} \quad (24a)$$

$$(\rho_f C_{pf})_{eff} = n_f S_{lf} \rho_l C_{pl} + n_f S_{gf} \rho_{gf} C_{pgf} \quad (24b)$$

$$(\rho_g C_{pg})_{eff} = S_{lf} \rho_l C_{pl} + S_{gf} \rho_{gf} C_{pgf} \quad (24c)$$

where C_{ps} and C_{pl} is the specific heat capacities of solid phase and water, respectively, C_{pa} and ρ_a the specific heat capacities of the adsorbed phase gas, $\rho_{g\alpha} = \left(\sum_{i=1}^{n_g} c_{ga}^i M^i\right)$, is the density of the gas mixture, M^i is the molar mass of i^{th} gas component and $C_{pg\alpha}$ is specific heat capacity of the gas mixture, which can be calculated as:

$$C_{pg\alpha} = \sum_{i=1}^{n_g} X_\alpha^i C_{pg\alpha}^i \quad (25)$$

where X_α^i is the mass fraction of i^{th} gas component, which is calculated as:

$$X_{\alpha}^i = \frac{x_{\alpha}^i M^i}{\sum_{i=1}^{n_g} x_{\alpha}^i M^i} \quad (26)$$

Unlike the effective specific heat capacity, for which an arithmetic mean is used, the effective thermal conductivity is obtained based on the geometric mean of the thermal conductivities of the three phases (Sass et al., 1971):

$$\lambda_{me} = \lambda_s^{(1-n_m-n_f)} \lambda_l^{n_m S_{lm}} \lambda_g^{n_m(1-S_{lm})} \quad (27)$$

$$\lambda_{ef} = \lambda_l^{n_f S_{lf}} \lambda_g^{n_f(1-S_{lf})} \quad \text{and} \quad \lambda_{eF} = \lambda_l^{S_{lf}} \lambda_g^{(1-S_{lf})} \quad (28)$$

where λ_s , λ_l and $\lambda_{g\alpha} = \sum_{i=1}^{n_g} X_{\alpha i} \lambda_g^i$ are the thermal conductivities of the solid, water and gas phases, respectively.

Heat transfer is separated into two processes, namely, heat transfer between the rock matrix and fracture fluid by conduction through the fracture surfaces, and heat transfer by advection through mass exchange between the continua (Heinze and Hamidi, 2017), given as:

$$q_{F-m} = h_T A_{fm} (T_f - T_m) + (\Gamma_{fjm} C_{pl} + \Gamma_{gfm} C_{pg}) (T_f - T_m) \quad (29)$$

where h_T is the heat transfer coefficient between the fracture and matrix continua, and A_{fm} is the interfacial fracture-matrix specific area, which can be estimated based on the geometric relation between the natural fractures and the rock matrix. The first term on the right-hand side of eq. (29) represents the heat exchange between matrix and fracture continua by conduction through the fracture surfaces, and the second term represents heat transfer by advection through the mass exchange term (Hao et al., 2013). Both h_T and A_{fm} are important parameters, influencing fracture-matrix interactions. The heat transfer coefficient is typically calculated by harmonic averaging of the matrix-fracture thermal conductivity (Hao et al., 2013):

$$h_T = \frac{\lambda_{em} \lambda_{ef}}{l \lambda_{ef} + w \lambda_{em}} \quad (30)$$

The interfacial fracture-matrix specific area is derived using geometrical considerations for an aperture w and a matrix block length l_b (Heinze and Hamidi, 2017):

$$A_{fm} = \frac{8l_b}{(2l_b + w)^2} \quad (31)$$

2.3. Deformation

The deformation behaviour of fractured rock is represented using dual poroelastic theory. The three basic principles of poroelastic theory, namely, the stress equilibrium, strain-displacement, and strain-stress relations are used. Based on the effective stress law, the total stress can be expressed in terms of the effective stress and the average pore pressure, as (Chen et al., 2019; Pao and Lewis, 2002):

$$d\sigma' = d\sigma - \alpha_m \mathbf{I} dp_m - \alpha_f \mathbf{I} dp_f \quad (32)$$

where σ is the total stress tensor, σ' is the effective stress tensor, \mathbf{m} is a vector with $\mathbf{m}^T = (1, 1, 1, 0, 0, 0)$ and $(1, 1, 0)$ for 3D and 2D problems, respectively, α_m and α_f are the Biot's effective stress coefficients of the matrix and matrix, respectively. p_m and p_f are the effective average pore pressures. For unsaturated fractured porous rock, the effective average pore pressure is weighted by the saturations for both the matrix and the fracture systems (Lewis and Schrefler, 1998; Pao and Lewis, 2002):

$$p_m = S_{lm} p_{lm} + S_{gm} p_{gm} \quad (33)$$

$$p_f = S_{lf} p_{lf} + S_{gf} p_{gf} \quad (34)$$

The Biot's effective stress coefficients, α_f and α_m , can be obtained in terms of physically measurable mechanical parameters (Lewis and Pao,

2002; Pao and Lewis, 2002), it can be shown that:

$$\alpha_f = 1 - \frac{K}{K_m} \quad (35)$$

$$\alpha_m = \frac{K}{K_m} - \frac{K}{K_s} \quad (36)$$

in which $K = E/3(1 - 2\nu)$, is the bulk modulus of fractured porous rock, and E is the Young's modulus, $K_m = E_m/3(1 - 2\nu)$, is the modulus of coal matrix with E_m being Young's modulus of the coal matrix, which can be obtained from the experiments performed on specimens an order of magnitude larger than the spacing of the matrix pores but devoid of fracture, and K_s is the modulus of solid constituent.

The stress-strain constitutive relation is defined as:

$$d\sigma' = \mathbf{D} d\epsilon^e \quad (37)$$

where \mathbf{D} is the elastic stiffness tensor.

The total strain can be expressed as:

$$d\epsilon = d\epsilon^e + \frac{1}{3} \mathbf{I} d\epsilon^s + \frac{1}{3} \mathbf{I} d\epsilon^T \quad (38)$$

where ϵ is the total strain vector, ϵ^e is the elastic strain vector, ϵ^s is the sorption-induced volumetric strain, and ϵ^T is thermal expansion-contraction strain.

The strain-displacement relation is written as:

$$d\epsilon = \mathbf{B} d\mathbf{u} \quad (39)$$

where \mathbf{u} is the solid displacement vector.

The thermal strain caused by temperature increases or decreases can be defined as:

$$\epsilon^T = \alpha_T (T - T_0) \quad (40)$$

where α_T is thermal expansion coefficient.

The total adsorption-induced strain is calculated using surface stress approach as:

$$\epsilon^s = -\frac{\alpha_m u_a}{K} \quad (41)$$

$$u_a = \zeta \Delta\sigma^s \quad (42)$$

where ζ is a material parameter representing the correlations between adsorption area variations of the matrix pore and in porosity of the matrix (Nikoosokhan et al., 2013). $\Delta\sigma^s$ is the change in surface stress due to gas adsorption. For the case of a pure gas, the change in surface stress can be obtained according to the Gibbs-Duhem relation (Chen et al., 2019; Nikoosokhan et al., 2012):

$$\Delta\sigma^s = - \int_{u_{g0}}^{u_g} \Gamma \bar{V}_b du_{gm} \quad (43)$$

where Γ is the number of moles of fluid molecules adsorbed per unit area of the fluid-solid interface, and $\bar{V}_b = RT/u_{gm}$ is the molar volume of the bulk fluid. If the fluid adsorption obeys Langmuir isotherm, the change of surface stress is written as:

$$\Delta\sigma^s = -\frac{RT_m \sum_{i=1}^{n_g} \Gamma_i^{max} b_{Li} x_i}{\sum_{i=1}^{n_g} b_{Li} x_i} \ln \left(1 + p_{gm} \sum_{i=1}^{n_g} b_{Li} x_i \right) \quad (44)$$

2.4. Numerical solution

This section presents the implementation of numerical techniques to solve the governing equations of water flow, multicomponent gas transport, heat transfer and mechanical deformation. A Galerkin-based finite element method is used for the spatial discretisation of the

to achieve fast and accurate solutions for computationally expensive subsurface flow simulations. The solution algorithm is presented in Table 1.

3. Hybrid MPI/OPENMP parallelization scheme

Due to growing availability of inexpensive symmetric multi-processors (SMPs) and advances in high-speed network devices, most HPC machines have a cluster architecture consisting of hybrid shared and distributed memory systems. In HPC clusters, a large number of distributed computer nodes are linked through high performance networks and there is no global memory space across all nodes. They have a communication network to connect individual memory. But each computer node itself generally is a symmetric multiprocessor (SMP) system, on which shared memory architecture allow all the processors to access the global memory space (Smith and Bull, 2001; Wang et al., 2016). The commonly used data transferring model between nodes is message passing, which has been realized by many parallel programming tools, such as, Aggregate Remote Memory Copy Interface (ARMCI) (Nieplocha and Ju, 2000), Message Passing Interface (MPI) (Walker and Dongarra, 1996), Parallel virtual machine (PVM) (Geist et al., 1994). Among these parallel programming tools, MPI, as a distributed memory model with explicit control parallelism, is the most widely used parallel

programming tool when parallelizing scientific codes. Although the explicit parallelism often provides a better performance, some limitations cannot be neglected. For example, communication can create a large overhead, which needs to be minimised, and the code granularity often has to be large to minimise latency (Smith and Bull, 2001). It is generally not an efficient technique within a SMP node. In contrast, a shared memory parallel programming model with implicit messaging like OpenMP can make a better use of the shared memory architecture (Castro et al., 2009). The programs using OpenMP can create threads and transform into multithreaded programs where the threads share the same memory address space and therefore the communications between threads are highly efficient. OpenMP offers a more efficient parallelization strategy for fine grain parallelism. In this work, both MPI and OpenMP are adopted for parallel implementation of the numerical code COMPASS to exploit the benefits of both models.

The major components of a finite element analysis are: initialization, global matrix build, matrix solution and update. For most problems, the time consumed by global matrix build and matrix solution accounts for the majority of simulation time (Mahinthakumar and Saied, 2002; Vardon et al., 2009; Wang et al., 2016). Thus, implementing parallel computing at these two stages significantly reduces the computational time.

Assembly of global matrix involves computation of local element

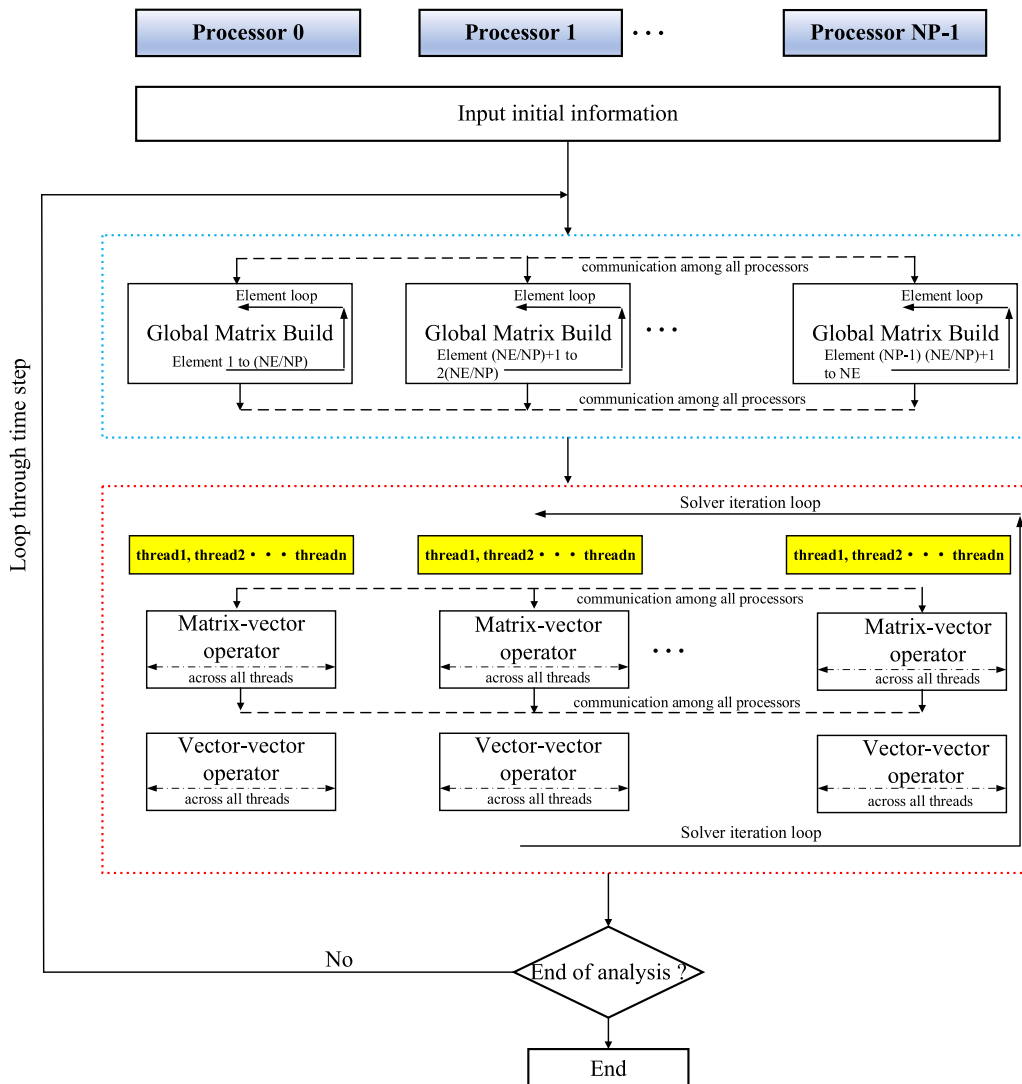


Fig. 4. Schematics of parallel finite element computations.

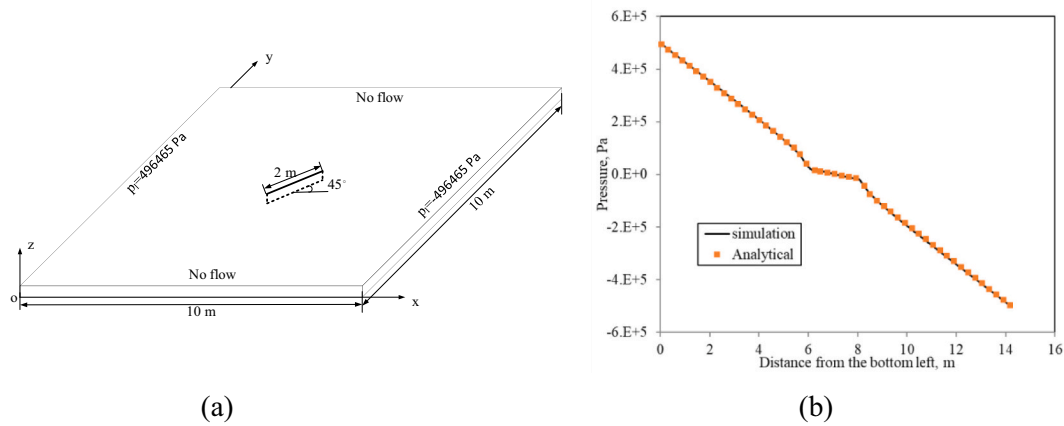


Fig. 5. (a) Computational domain embedded with a discrete fracture and boundary conditions for verification test and (b) Comparison of analytical solution and numerical result for the pressure profile along a diagonal line from the bottom-left to the top-right of the domain.

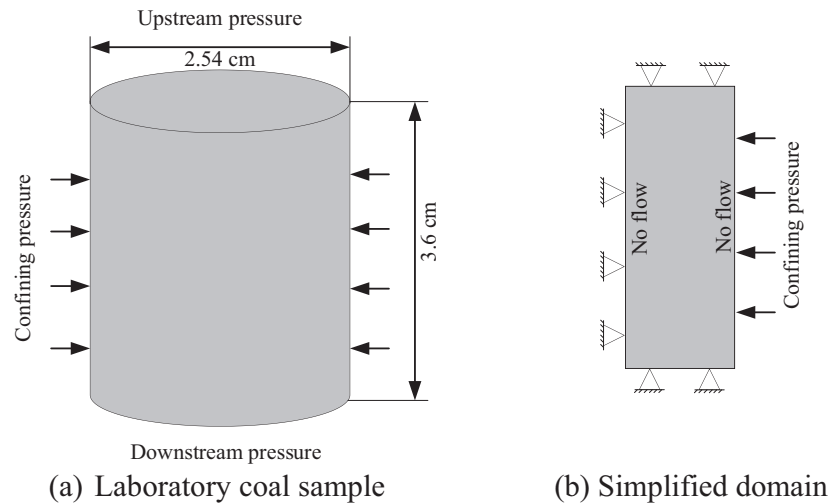


Fig. 6. Geometry and boundary conditions for matching of an experiment performed by Pini et al. (2009).

matrices and addition to a global matrix. All information required to complete this step is known at the start of each iteration, and there is no need for communication for each element matrix calculation within each iteration. Therefore, coarse-grained domain decomposition can be employed, meaning that the number of finite elements (NE) is split over the number of processing cores (NP). After completion of each element matrix, the MPI collective communication calls are used to assemble all element matrices together and form the global matrix for solution.

The solver section solves the global matrix by using a preconditioned BiCGSTAB solver which is mentioned earlier and shown in Table 1. The sparse matrix-vector multiplication and vector-vector operations are the most computationally intensive operations in this algorithm (Mahinthakumar and Saied, 2002). Coarse grained parallelism is used for the matrix-vector multiplication, which is carried out across nodes of a cluster using MPI. The vector-vector operations are relatively simple. In this case parallelizing using MPI is not suitable as the communication may take longer than the calculation itself. However, OpenMP provides efficient, fine-grained parallelism (Mahinthakumar and Saied, 2002; Vardon et al., 2009; Wang et al., 2016). Fig. 4 shows an overview of the hybrid parallel computing scheme used in this work. Hybrid parallel computation is performed by MPI between nodes and by OpenMP within each node.

4. Model verification and validation

In this section, the parallel hybrid discrete fracture – dual continuum model is tested against an analytical solution and a laboratory experiment to demonstrate implementation accuracy and reliability of the proposed model to interpret underlying physical processes. The analytical solution derived by Strack (1982) and laboratory tests by Pini et al. (2009) are used as the benchmarks for model evaluation. More verification and validation exercises can be found in our previous work (e.g. Chen, 2019; Chen et al., 2020a; Chen et al., 2022; Hosking et al., 2020), including unsaturated flow, THM coupling, dynamic fracture aperture, adsorption induced deformation, stress dependent permeability, historical matching of field production data, and so forth.

Firstly, for comparison against the analytical solution, 3D infinite horizontal plane with an embedded fracture is considered. The midpoint of the discrete fracture coincides with the centre of the plane, as shown in Fig. 5 (a). The discrete fracture has a length of 2 m and is inclined at an angle of 45° with aperture of 0.05 m, represented as a 2D geometry. The prescribed water pressures at the lateral boundaries are 496,465 Pa and $-496,465$ Pa, respectively and zero flux is assigned to the top and bottom boundaries. The matrix permeability is 1.0×10^{-8} m² and viscosity of water is 1.0×10^{-3} Pa·s, which are chosen from (Chen, 2019). Pressure distribution along a diagonal line from the bottom-left to the top-right of the domain at steady state is shown in Fig. 5(b).

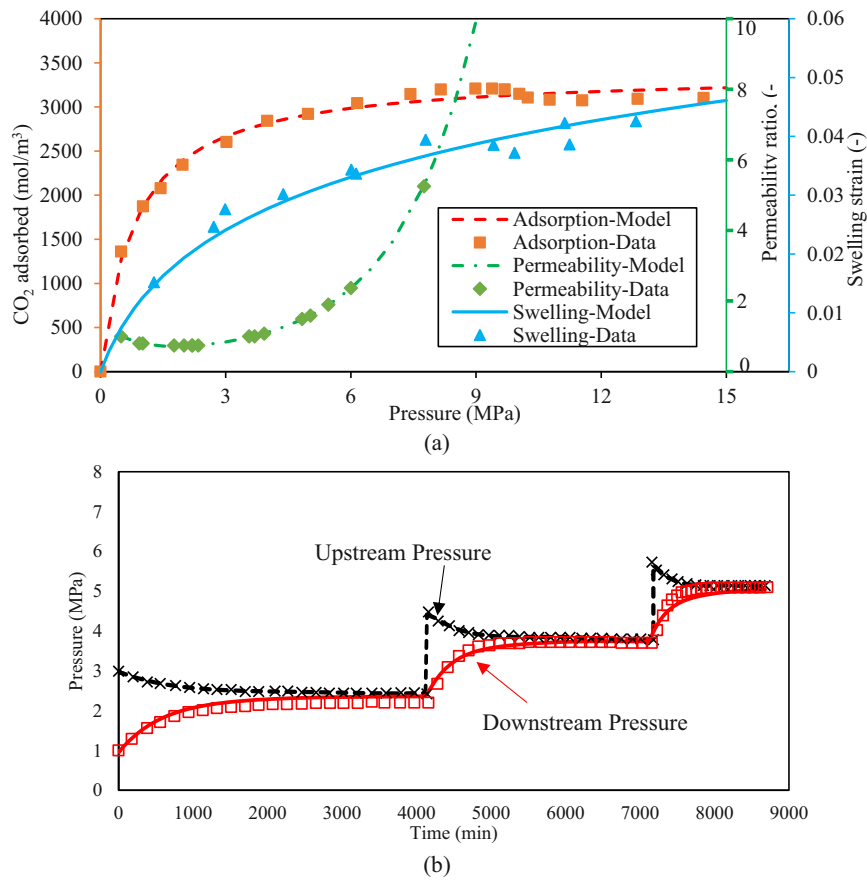


Fig. 7. (a) Comparison of CO₂ adsorption, swelling strain, permeability evolution predicted by the model against the experimental data of Pini et al. (2009), and (b) Comparisons between model results (lines) and experimental measurements (symbols) of the upstream and downstream pressure.

Table 2
Model inputs used for the validation test against data by Pini et al. (2009).

Material parameters	Value	Source
Young's modulus of coal, E (GPa)	1.12	Pini et al. (2009)
Matrix modulus, K_m (GPa)	10.34	Hosking et al. (2020)
Poisson's ratio, ν (-)	0.26	Pini et al. (2009)
Initial permeability, K_{f0} (m ²)	1.1×10^{-19}	Pini et al. (2009)
Initial matrix porosity n_{m0} (-)	0.02	Pini et al. (2009)
Initial fracture porosity n_{f0} (-)	0.0042	Pini et al. (2009)
Density of coal, ρ_s (kg/m ³)	1356.6	Pini et al. (2009)
Langmuir volume constant, c_L (mol/kg)	2.49	Pini et al. (2009)
Langmuir pressure, b_L (MPa ⁻¹)	1.25	Pini et al. (2009)
Fracture compressibility, C_{pf0} (MPa ⁻¹)	0.092	Fitting
Mass exchange coefficient, σ_{gD} (s ⁻¹)	3.9×10^{-6}	Hosking et al. (2020)
Temperature, T (K)	318.15	Pini et al. (2009)

The results show a good agreement with the analytical solution, demonstrating the correctness of the implementation of developed model. For verification of parallelized code, the coefficient matrix and right hand side vector (Eq. 47) calculated by both serial and parallel versions are compared, the values are almost the same. The numerical solutions obtained from both versions were also compared against each other.

Secondly, Pini et al. (2009) performed gas injection (He, N₂ and CO₂) experiments on coal cores with transient step method. The coal core was 2.54 cm in diameter and 3.6 cm in length, injection pressures ranged from 1 MPa to 8 MPa under constant and varying confining pressure. The results for CO₂ under a constant confining pressure were collected as benchmarks for validation of the numerical model in terms of the gas flow in deformable coals. Fig. 6 (a) shows the schematic of the coal core

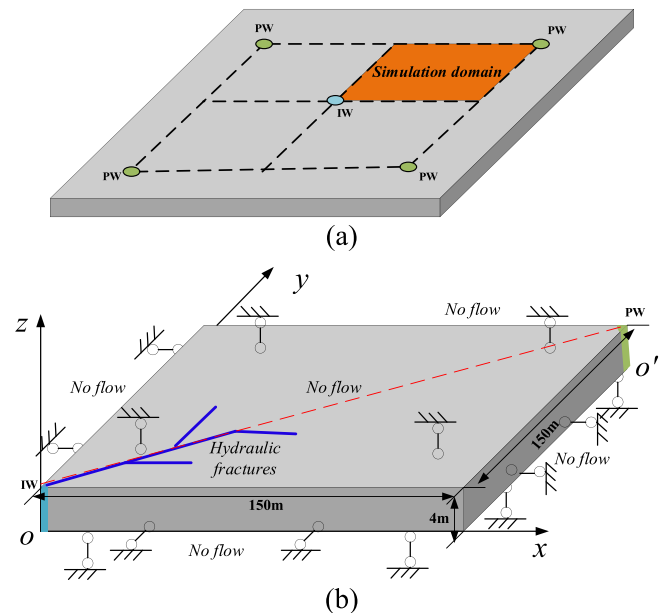


Fig. 8. Schematic of the model domain and boundary conditions.

used by Pini et al. (2009), which is simplified to the simulation domain shown in Fig. 6(b) via principle of axisymmetry. No flow boundaries are used along the left- and right-hand sides of the domain. A time-dependent upstream CO₂ injection pressure (see Fig. 7b) is prescribed

on top boundary, whilst for coal deformation a vertical constraint is applied to upstream and downstream boundaries, no horizontal displacement is assigned to left-hand side of the domain with a constant confining stress of 10 MPa at the right-hand boundary, as shown in Fig. 6 (b). The initial pressure is 1 MPa. The material parameters used for this test are provided in Table 2. The permeability evolution is captured by the stress dependent permeability model presented in the previous work (Chen et al., 2022), fracture compressibility is obtained by matching the permeability data by Pini et al. (2009).

Comparisons of adsorption, coal swelling, permeability variation with pressure and transient downstream pressure predicted by developed model against the experimental measurements are shown in Fig. 7. It can be seen that the developed model can successfully capture the CO₂ flow dynamics in coal at the laboratory scale under the conditions considered, which indicates the ability of model to interpret the underlying physical processes.

5. Application of numerical model to CO₂ sequestration in coals

CO₂ sequestration in coal seams is a potential technique to reduce CO₂ emission into atmosphere since CO₂ adsorption capacity of coal is stronger, and at the same time, coalbed methane (CBM) is displaced, improving the CBM production, this process is known as CO₂-enhanced coalbed methane recovery (CO₂-ECBM). In this section, the parallel code is applied to CO₂-ECBM recovery simulation scenario. CO₂ injection, storage, and coalbed methane displacement in a fractured coalbed is modelled using the integrated dual continuum and discrete fracture model presented in Section 2. This application example will be used to assess improvement of performance of developed parallel finite element scheme for simulating large spatio-temporal THCM coupling problem in the following section.

5.1. Computing platform

The simulations presented in this work were performed on a Linux

Table 3
Model parameters for simulations of CO₂-ECBM recovery.

Material parameters	Value
Bulk modulus of coal, K (GPa)	2.1
Bulk modulus of coal matrix, K_m (Gpa)	14.3
Bulk modulus of coal solid, K_s (Gpa)	29.0
Poisson's ratio, ν (-)	0.32
Coal density, ρ_s (kg/m ³)	1470
Initial fracture porosity, n_{f0} (-)	0.018
Initial matrix porosity, n_{m0} (-)	0.045
Initial permeability, k_{f0} (m ²)	1.5e-15
Cleat compressibility, C_{pf} , MPa ⁻¹	0.029
Initial saturation, $S_{w,-}$	0.9
Interaction energy of CH ₄ , E_m (J/mol)	9238
Reduction coefficient of CH ₄ , δ (K ⁻¹)	0.0083
Interaction energy of CO ₂ , E_m (J/mol)	5266
Reduction coefficient of CO ₂ , δ (K ⁻¹)	0.023
Langmuir pressure constant for CO ₂ , b_L (MPa ⁻¹)	0.73
Langmuir constant for CO ₂ , c_L (mol/kg)	1.5
Langmuir pressure constant for CH ₄ , b_L (MPa ⁻¹)	0.5
Langmuir constant for CH ₄ , c_L (mol/kg)	0.63
Moisture induced reduction coefficient of CH ₄ , ξ (-)	0.145
Moisture induced reduction coefficient of CO ₂ , ξ (-)	0.172
Thermal expansion coefficient, α_T (K ⁻¹)	9.0e-5
Thermal conductivity of CO ₂ , λ_g (W/m/K)	0.0246
Thermal conductivity of CH ₄ , λ_g (W/m/K)	0.0371
Thermal conductivity of coal, λ_s (W/m/K)	0.33
Specific heat capacity of coal, C_{ps} (J/K/kg)	1250
Specific heat capacity of water, C_{pw} (J/K/kg)	4200
Thermal expansion coefficient of water, α_{T1} (1/K)	6.9 × 10 ⁻⁵
Saturation constant, γ (-)	4.25
Saturation constant, p_0 (Pa)	2.5e4
Water viscosity, μ_1 (Pa·s)	1.0e-3
Matrix block length, l_b (m)	0.01

based HPC cluster, Hawk, located at Cardiff University, UK. Hawk Linux cluster comprises of both Intel Skylake Gold (2.4GHz / 4.8GB per core / 20 cores per processor) and AMD nodes comprising dual AMD EPYC Rome 7502 processors (2.5 GHz / 4.0 GB per core / 32 cores per processor). Hawk includes Intel Skylake Gold 6148 processors as the main parallel MPI partition (including a High Memory, SMP section), as well as dual processor AMD Rome 7502 nodes providing X86-64 capability, plus additional Intel Skylake Gold as a serial/high throughput subsystem. Nodes are connected with InfiniBand EDR technology (100 Gbps/ 1.0 μ s latency) from Mellanox. More details can be found in <https://www.cardiff.ac.uk/advanced-research-computing/about-us/our-supercomputers>. In this study, the Intel Skylake Gold processors are used.

5.2. Simulation setup

A typical five-well layout is usually designed for CO₂-ECBM recovery (Ma et al., 2017), as shown in Fig. 8(a). In this layout, the CO₂ injection well (IW) is drilled at the centre of a near-square array composed of four production wells (PW). Due to symmetry, only a quarter of the 3D reservoir domain represented by a 150 m × 150 m × 4 m block shown in Fig. 8(b), is considered in the simulation. Z-direction is perpendicular to the coal bedding-plane and the coal-seam is 4 m in thickness at a depth of 400 m. It is assumed that prior to infection there is no CO₂ present in the model domain. The initial reservoir pressure and temperature are 4.0 MPa and 303 K, respectively. The initial vertical stress and horizontal stress are estimated to be 9 MPa and 6.3 MPa according to depth. A zero-flux boundary is applied at the external boundaries for water and gas flow, with the fixed pressure of 0.1 MPa for the production well. The gas pressure boundary and initial gas pressure were converted into the equivalent free gas concentrations using the real gas law in simulation. For coal deformation, a constant volume condition is applied, as shown in Fig. 7(b). The model domain is discretized by 201,846 tetrahedra elements containing a total of 472,355 degrees of freedom. The CO₂ injection pressure is set 6 MPa. The simulation parameters are listed in Table 3.

5.3. Simulation results

Fig. 9 shows the spatial distribution of free phase CO₂ and CH₄ after 90 days and 180 days of CO₂ injection. Due to higher conductivity of hydraulic fractures, CO₂ prefers to flow within the hydraulic fracture, and then it migrates from hydraulic fractures into surrounding domain. The gas phase CO₂ concentration in hydraulic fractures is almost identical to the injection well, as shown in Fig. 11. With continuous injection of CO₂, exiting free CH₄ is driven by CO₂ and advances toward production well, as illustrated in Fig. 9(b). It is evident that the displaced CH₄ accumulate in the vicinity of the advancing CO₂ front which contributes to CH₄ recovery, as higher pressure gradient forms toward the production well.

To demonstrate the role of hydraulic fractures, a simulation scenario in absence of hydraulic fractures is simulated for comparison. After 180 days of CO₂ injection, gas phase CO₂ and CH₄ concentration contour plots without hydraulic fractures are presented in Fig. 10. It can be seen that the injected CO₂ flows, radially, away from the injection well in this case, which produces a uniform CO₂ distribution around the injection well. The spread of CO₂ in the domain is also much smaller than that with considering hydraulic fractures. The gas phase CH₄ concentration at the advancing CO₂ front reaches to 2450 mol/m³ after 180 days when considering hydraulic fractures, whereas the concentration is roughly 1726 mol/m³ when hydraulic fractures are ignored. Fig. 11 compares the gas phase concentration distributions of CO₂ and CH₄ along the diagonal length of the domain (marked by dotted lines in Fig. 8b) after 90 days and 180 days of CO₂ injection. It can be observed that when hydraulic fractures are absent, the accumulation of CH₄ at the advancing CO₂ front is far less than that with considering hydraulic fractures, this is

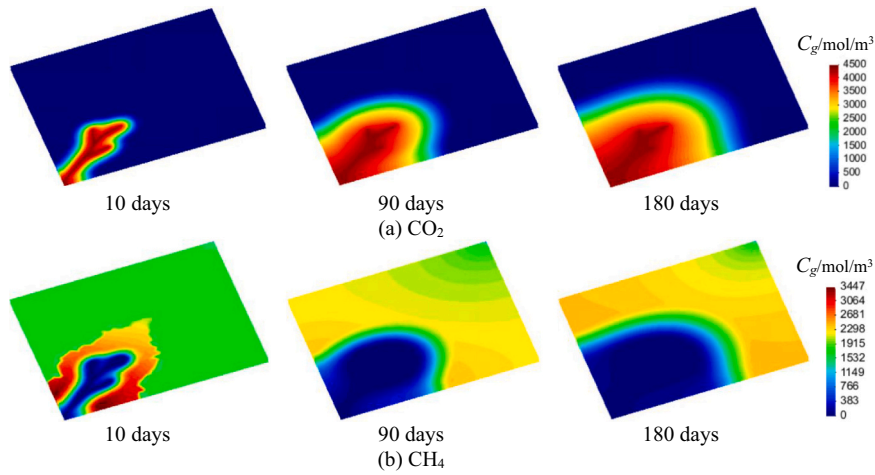


Fig. 9. Spatial distribution of gas phase CO₂ and CH₄ concentration after 90 days and 180 days.

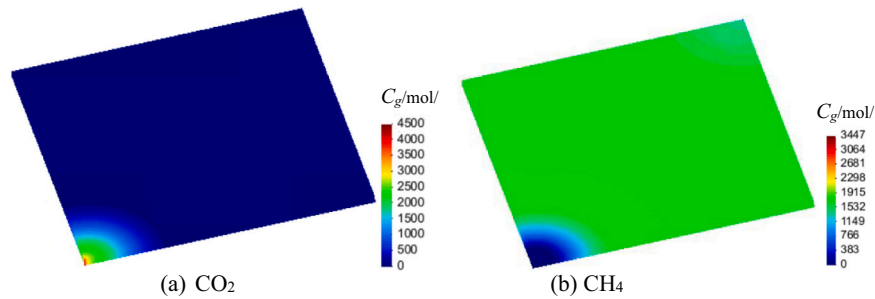


Fig. 10. Spatial distribution of gas phase CO₂ and CH₄ concentrations ignoring hydraulic fractures. The results are plotted after 180 days of simulation.

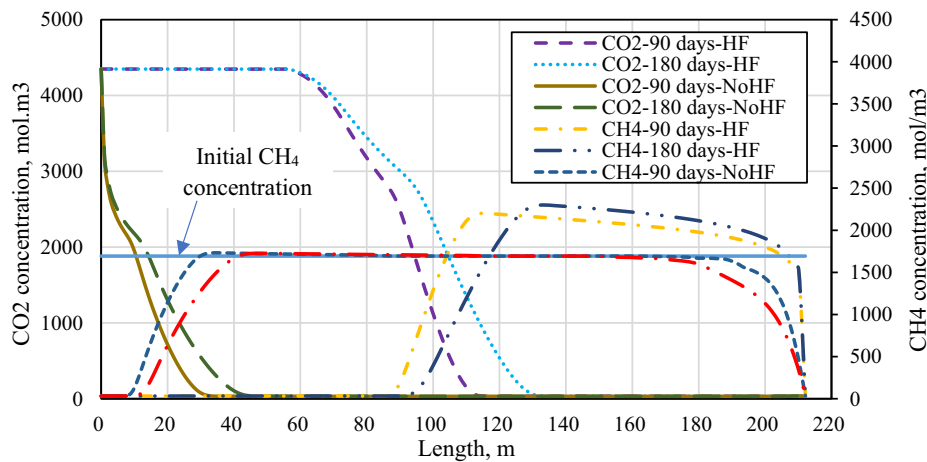


Fig. 11. Evolution of gas phase CO₂ and CH₄ concentration profiles along the diagonal OO'.after 90 and 180 days (HF and NoHF denote presence and absence of hydraulic fractures, respectively).

because less CO₂ is injected into the coal seam, leading to less CH₄ displacement. The CH₄ concentration distributions in the vicinity of production well are also different, i.e. its concentration in this region when considering hydraulic fractures is higher than that without hydraulic fractures. The spatial distributions of adsorbed phase CO₂ and CH₄ concentrations are similar to gas phase CO₂ and CH₄ concentration and not presented here.

Fig. 12(a) shows the spatial distribution of water saturation after 30 days, 90 days of CO₂ injection. Since, the CO₂ injection pressure is higher than the reservoir pressure, the injected CO₂ drives the formation

water away from the injection well. After 90 days of injection, the mobile/ free water is drained and the seam reaches to the residual water saturation level. This is consistent with field observations in the field test, where water production rate is higher only at early stage of injection. Fig. 12 (b) demonstrates the temperature evolution of coalbed along the diagonal length of the domain. Since the temperature of injected CO₂ is lower than that of the coalbed, the temperature of coalbed decreases with continuous gas injection. As a response to gas adsorption/desorption-induced swelling/shrinkage, the coal permeability could experience dramatic alteration. As shown in Fig. 12(c), in

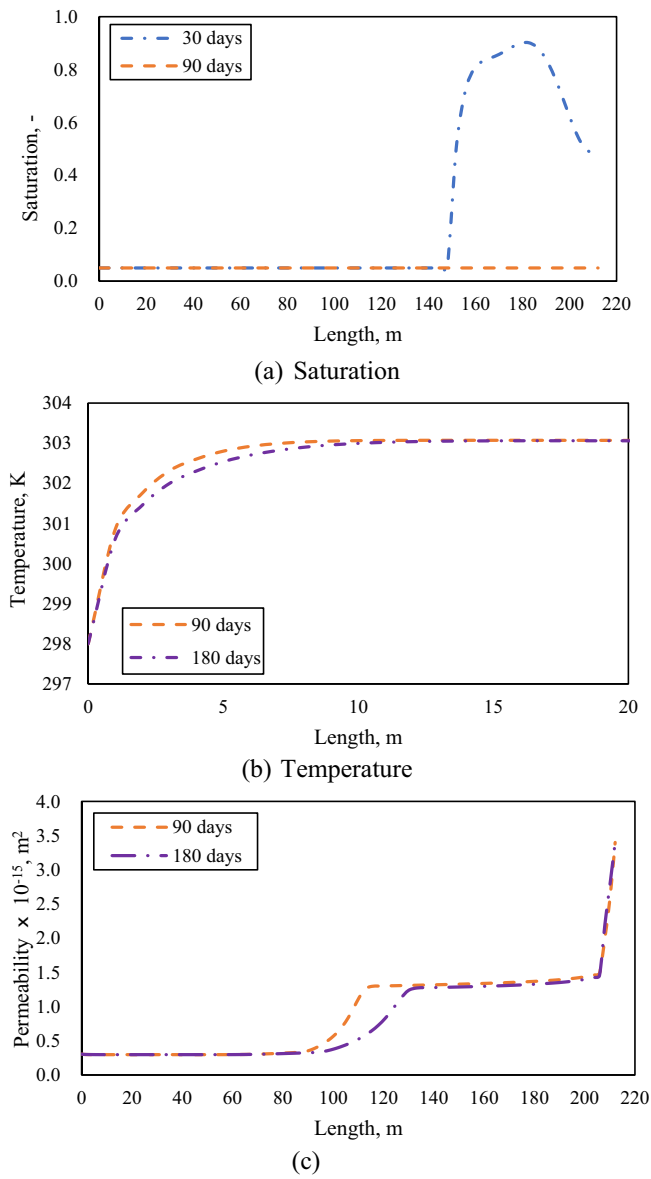


Fig. 12. Spatial distribution of saturation (a), temperature (b) and permeability (c) along the diagonal OO'.

the region where CO₂ reached, the coal permeability has dropped significantly from 1.5 mD to 0.3 mD due to CO₂ induced coal swelling. However, the coal permeability in the vicinity of production well undergoes an increase. This is because CH₄ desorption from the coal matrix causes coal matrix shrinkage, which results into increase in the fracture permeability.

6. Results and discussions

Here, computational efficiency of the proposed parallel scheme developed for the coupled THCM model (Section 2) is analysed and discussed by focusing on the application example presented in the previous section. The wall-clock time, which is defined as the time that has elapsed between the start and end of the code execution, is used to assess the performance of the parallel scheme. The time spent on the system matrix formation and solution for discretised equations has been calculated. For initial performance test, parallel simulations have been carried out using 2, 4, 6, 8, 12 and 24 Intel processing cores for MPI parallelization and 2, 6 and 10 cores for OpenMP threads, each case is

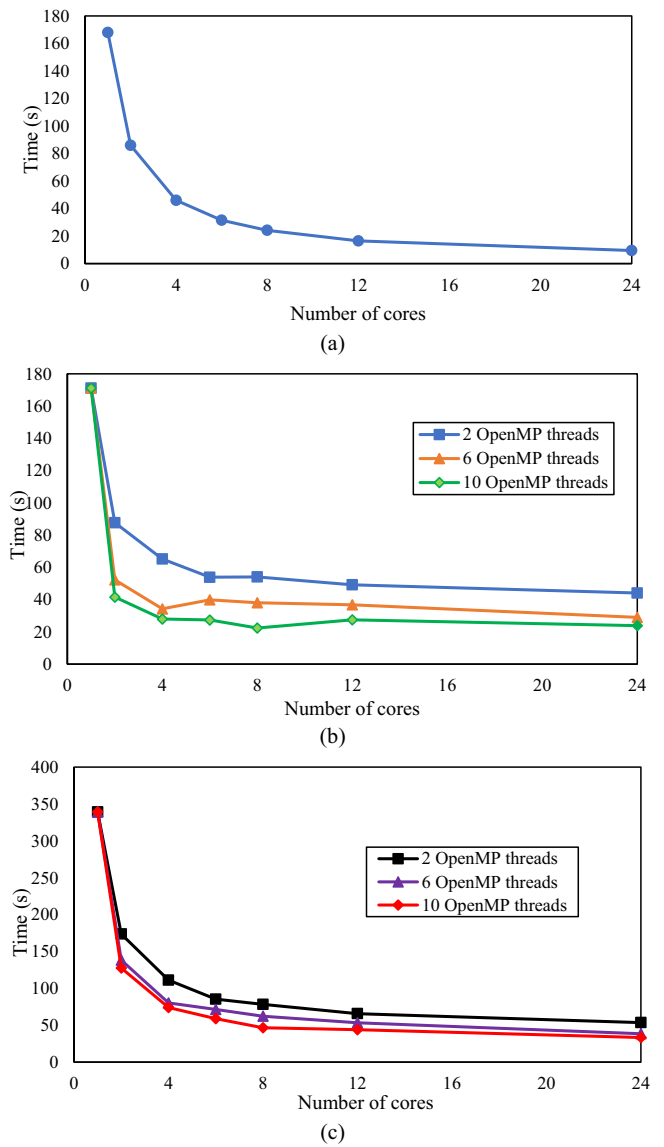


Fig. 13. (a) Wall time of system matrix build with various MPI processes, (b) Wall time of solver with various number of MPI processes and OpenMP threads and (c) Total wall time of system matrix build and solver.

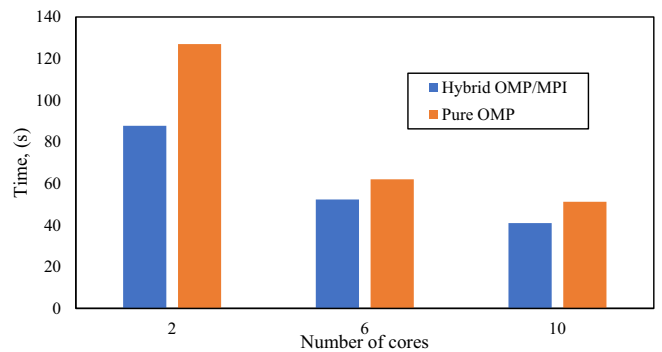


Fig. 14. Comparison of wall time of solver parallelized with pure OpenMP and hybrid OpenMP/MPI.

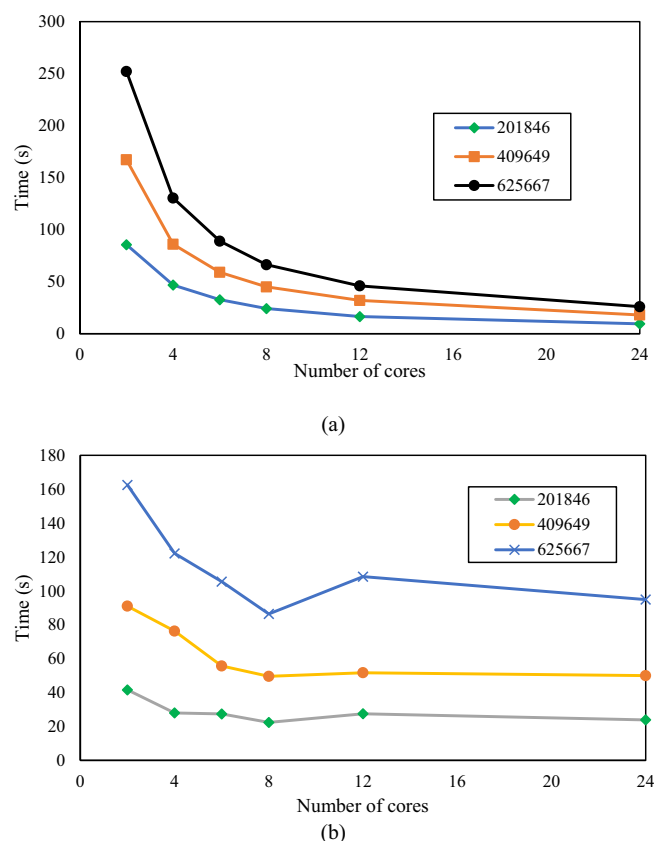


Fig. 15. Comparison of wall times of system matrix build and solver for different size simulations.

run for 5 timesteps only.

The computational performance of system-matrix build against the number of processing cores is shown in Fig. 13(a). Here it is worth pointing out that the wall time against 1 core in following plots refers to serial execution time, that was obtained by executing serial code. It can be seen from Fig. 13 that the parallel scheme for system matrix build shows an excellent improvement with increase in the number of involved processing cores. For serial implementation, the time spent on system matrix formation is 168 s. A satisfactory scalability is achieved when the number of processors increases to 8. The wall time for system matrix build is reduced from 86 s to 24 s. The speedup, which is defined as the ratio of run time of a serial implementation by running time of parallel execution (Pacheco, 2011), increases from 1.95 to 6.5 to the parallel efficiency, which is computed as the speedup divided by involved number of processing cores (Pacheco, 2011), drops from 97.5% to 87%, which is close to an linear speedup (100%). Although the execution speed increases with the number of assigned cores (16.5 s and 9.6 s for 12 and 24 cores, respectively), the efficiency decreases (85% and 73% for 12 and 24 cores, respectively). This is because communication cost of MPI increases with the number of processors, in particular, when more than one nodes are involved, speed up is reduced (Mahinthakumar and Saied, 2002; Vardon et al., 2011).

Fig. 13(b) shows the performance efficiency of the parallel solver algorithm. The solver mainly performs vector-vector and matrix-vector operations, which are parallelized with OpenMP and MPI, respectively. Solver performance with various MPI processes and OpenMP threads is tested. Overall, the time for solver decreases with increase in number of OpenMP threads. The wall time for serial implementation is 171 s, as shown in Fig. 13(b), which is reduced significantly for hybrid parallelized execution. When 4 MPI processes are used, the wall time for solver is 65 s, 34 s and 28 s and the speedups are 2.6, 5.0 and 6.1 for 2, 6

and 10 OpenMP threads, respectively. Although the wall time is reduced with increasing number of threads, speed-up increase slow down. This may be because multiple threads access the same shared array and cause synchronization overheads. When the number of OpenMP threads remains constant, the speedup increase is hardly possible when more than 8 MPI processes are used, especially when more OpenMP threads are used, even speedup drop occurs because of increasing cost of MPI communications with MPI processes. This also indicates that the vector-vector operations within each node are dominant in the solving process. This is also realized by the fact that the running time of solver drops with increase in OpenMP threads as MPI processes remain constant.

The total wall time for system matrix build and solver is illustrated in Fig. 13(c). Since the time required for global matrix formation and solver is reduced, the total time of the parallel scheme is also be reduced. It requires only 34 s comparing to 339 s required for serial implementation with about 10 speedup. The performance efficiency of parallelized solver is also examined. The parallel computations of solver with pure OpenMP are considered as benchmark. 2 MPI processes are used for parallelized solver with a hybrid approach. Fig. 14 shows the comparison of wall time spent on solution for different parallel schemes of solver. It is found that the mixed MPI/OpenMP model performs better than pure OpenMP on such architectures, similar results were also reported by Lanucara and Rovida (1999).

In addition to examining the performance of parallel implementation with respect to number of processing cores, the performance of hybrid approach for different simulation sizes are also investigated. To this end, another two finer spatial discretizations were selected for the analysis, the grid is refined with 401,649 and 625,667 tetrahedra elements (approximate fold increase). Due to insufficient memory of a core for simulation domain discretised with 625,667 tetrahedra elements, the time for two MPI processes is selected as benchmark. Fig. 15 shows the time spent on matrix build and solving the system of equations. For two MPI processors, the times on matrix build are 86 s, 167 s and 252 s for three different size simulations, respectively, as shown in Fig. 15(a). With an increase to 24 cores for MPI process, the times on matrix build decrease to 10 s, 18 s and 26 s, respectively. The ratio of time for 2 cores to 24 cores are 8.6, 9.3 and 9.7 for three different size simulations, respectively. This implies that with increasing simulation size, the speedup for matrix build increases, similar observation was also reported in literature (e.g. Pacheco, 2011; Su et al., 2017). As shown in Fig. 15(b), although a slight increase in time of solver for 12 MPI processes is observed, the time on solver shows a drop with increase MPI processes. When MPI process increase to 8, the ratios of time for 2 MPI processes to 8 MPI processes are 1.86, 1.83 and 1.88 for the three sizes investigated here, respectively. These results show a satisfactory scalability of the adopted parallel scheme.

7. Conclusions

To improve computational efficiency of a numerical model that is developed to study CO₂ storage and ECBM recovery in naturally fractured reservoirs such as coal and shale deposits, this work presents a comprehensive description of a hybrid dual continuum and discrete fracture model with detailed procedure for implementing a high-performance parallel scheme. In the model, large scale fractures are represented explicitly with discrete fracture model and treated as a lower dimensional object. Numerous small scale fractures and porous matrices are modelled using dual porosity approach. The principle of superposition is employed to achieve the coupling between both modelling approaches. Hybrid dimensional elements are used for spatial discretization. Lower dimensional interface element sharing the same nodes between the two continua is used to discretize the large scale fractures. In order to facilitate numerical modelling of large-scale, long-term computationally intensive problems, a hybrid MPI/OpenMP parallel scheme is designed and has been implemented into the in-house finite element based modelling code, where the code for finite element

matrix build is parallelized with MPI communication operations and the parallelization of codes for vector-vector and matrix-vector operations of the biconjugate gradient stabilized (BiCGSTAB) solver are achieved via OpenMP and MPI implementation, respectively.

The model is evaluated against an analytical solution and a laboratory experiment to demonstrate its reliability and implementation accuracy. Performance and computational efficiency of the proposed parallel scheme are analysed by 3D modelling CO₂ sequestration and enhanced coalbed methane recovery. The simulation results show that the proposed model is able to capture the role of large scale fracture and coupled behaviour during CO₂ injection in coal reservoirs. The performance test of the present parallel scheme show that it can provide a significant improvement compared to the serial implementation. The speedup of up to about 10 times and satisfactory scalability have been achieved for considered model problem. The developments presented in this work provides an efficient computational tool for 3D dimensional modelling of large scale coupled processes in fractured porous media with complex fracture systems.

CRedit authorship contribution statement

Min Chen: Conceptualization, Data curation, Formal analysis,

Writing – original draft, Methodology, Validation, Investigation, Software. **Shakil Masum:** Writing – review & editing, Project administration. **Hywel Thomas:** Funding acquisition, Supervision.

Declaration of Competing Interest

The authors declare that they have no known competing financial interests or personal relationships that could have appeared to influence the work reported in this paper.

Acknowledgement

The research was conducted as part of the “Establishing a Research Observatory to Unlock European Coal Seams for Carbon Dioxide Storage (ROCCS)” project. The ROCCS project has received funding from the Research Fund for Coal and Steel under Grant Agreement No. 899336. The financial support is gratefully acknowledged. Support and use of the computing facilities at Advanced Research Computing @ Cardiff (ARCCA) at Cardiff University are also gratefully acknowledged.

Appendix A

$$C_{ll,m} = \sum_{e=1}^{n_{ele}} \int_{\Omega^e} \left[n_m \left(S_{lm} c_l - \frac{\partial S_{lm}}{\partial p_{cm}} \right) N^T N \right] d\Omega^e$$

$$C_{lc_g^i,m} = \sum_{e=1}^{n_{ele}} \int_{\Omega^e} \left[n_m Z_m R T_m \frac{\partial S_{lm}}{\partial p_{cm}} N^T N \right] d\Omega^e$$

$$C_{IT,m} = \sum_{e=1}^{n_{ele}} \int_{\Omega^e} \left[n_m \left(R Z_m \frac{\partial S_{lm}}{\partial p_{cm}} \sum_{i=1}^{n_g} c_m^i - S_{lm} \alpha_{IT} \right) N^T N \right] d\Omega^e$$

$$C_{ll,f+F} = \sum_{e=1}^{n_{ele}} \int_{\Omega^e} \left[n_f \left(S_{lf} c_l - \frac{\partial S_{lf}}{\partial p_{cf}} \right) N^T N \right] d\Omega^e + \sum_{e=1}^{n_{eleF}} \int_{\Gamma^{Fe}} \left[w \left(S_{IF} c_l - \frac{\partial S_{IF}}{\partial p_{cF}} \right) N_F^T R^T R N_F \right] d\Gamma^{Fe}$$

$$C_{lc_g^i,f+F} = \sum_{e=1}^{n_{ele}} \int_{\Omega^e} \left[n_f Z_f R T_f \frac{\partial S_{lf}}{\partial p_{cf}} N^T N \right] d\Omega^e + \sum_{e=1}^{n_{eleF}} \int_{\Gamma^{Fe}} \left[w Z_f R T_f \frac{\partial S_{IF}}{\partial p_{cF}} N_F^T R^T R N_F \right] d\Gamma^{Fe}$$

$$C_{IT,f+F} = \sum_{e=1}^{n_{ele}} \int_{\Omega^e} \left[n_f \left(R Z_f \frac{\partial S_{lf}}{\partial p_{cf}} \sum_{i=1}^{n_g} c_f^i - S_{lf} \alpha_{IT} \right) N^T N \right] d\Omega^e + \sum_{e=1}^{n_{eleF}} \int_{\Gamma^{Fe}} \left[\left(R Z_f \frac{\partial S_{IF}}{\partial p_{cF}} \sum_{i=1}^{n_g} c_f^i - S_{IF} \alpha_{IT} \right) N_F^T R^T R N_F \right] d\Gamma^{Fe}$$

$$C_{c_g^i,l,m} = \sum_{e=1}^{n_{ele}} \int_{\Omega^e} \left[\left((1 - H_g^i) n_m c_{gm}^i \frac{\partial S_{lm}}{\partial p_c} \right) N^T N \right] d\Omega^e$$

$$C_{c_g^i,c_g^j,m} = \sum_{e=1}^{n_{ele}} \int_{\Omega^e} \left[\left(\rho_s \frac{dc_s^j}{dc_{gm}^j} + n_m H_g^i \delta_{ij} + (1 - H_g^i) n_m S_{gm} \delta_{ij} - (1 - H_g^i) n_m c_{gm}^i T_m Z_m R \frac{\partial S_{lm}}{\partial p_{cm}} \right) N^T N \right] d\Omega^e$$

$$C_{c_g^i,T,m} = \sum_{e=1}^{n_{ele}} \int_{\Omega^e} \left[- (1 - H_g^i) n_m c_{gm}^i Z_m R \frac{\partial S_{lm}}{\partial p_{cm}} \sum_{i=1}^{n_g} c_m^i N^T N \right] d\Omega^e$$

$$C_{c_g^i,l,f+F} = \sum_{e=1}^{n_{ele}} \int_{\Omega^e} \left[\left((1 - H_g^i) n_f c_{gf}^i \frac{\partial S_{lf}}{\partial p_{cf}} \right) N^T N \right] d\Omega^e + \sum_{e=1}^{n_{eleF}} \int_{\Gamma^{Fe}} \left[\left((1 - H_g^i) w c_{gf}^i \frac{\partial S_{IF}}{\partial p_{cF}} \right) N_F^T R^T R N_F \right] d\Gamma^{Fe}$$

$$C_{c_g^i,c_g^j,f+F} = \sum_{e=1}^{n_{ele}} \int_{\Omega^e} \left[\left(n_f H_g^i \delta_{ij} + (1 - H_g^i) n_f S_{gf} \delta_{ij} - (1 - H_g^i) n_f c_{gf}^i T_f Z_f R \frac{\partial S_{lf}}{\partial p_{cf}} \right) N^T N \right] d\Omega^e + \sum_{e=1}^{n_{eleF}} \int_{\Gamma^{Fe}} \left[w \left(H_g^i \delta_{ij} + (1 - H_g^i) \left(S_{gF} \delta_{ij} - c_{gF}^i T_f Z_f R \frac{\partial S_{IF}}{\partial p_{cF}} \right) \right) N_F^T R^T R N_F \right] d\Gamma^{Fe}$$

$$\mathbf{C}_{c_g^i, T, f+F} = \sum_{e=1}^{n_{ele}} \int_{\Omega^e} \left[- \left(1 - H_g^i \right) n_f c_{gf}^i Z_f R \frac{\partial S_{lf}}{\partial p_{cf}} \sum_{i=1}^{n_g} c_f^i N^T N \right] d\Omega^e + \sum_{e=1}^{n_{eleF}} \int_{\Gamma^{Fe}} \left[- \left(1 - H_g^i \right) w c_{gf}^i Z_f R \frac{\partial S_{lf}}{\partial p_{cF}} \sum_{i=1}^{n_g} c_f^i N_F^T \mathbf{R}^T \mathbf{R} N_F \right] d\Gamma^{Fe}$$

$$\mathbf{C}_{TT, m} = \sum_{e=1}^{n_{ele}} \int_{\Omega^e} \left[\left(\left(\rho_m C_{pm} \right)_{\text{eff}} - n_m S_{gm} Z_m R \sum_{j=1}^{n_g} c_m^j \right) N^T N \right] d\Omega^e$$

$$\mathbf{C}_{TT, f+F} = \sum_{e=1}^{n_{ele}} \int_{\Omega^e} \left[\left(\left(\rho_f C_{pf} \right)_{\text{eff}} - n_f S_{gf} Z_f R \sum_{j=1}^{n_g} c_f^j \right) N^T N \right] d\Omega^e + \sum_{e=1}^{n_{eleF}} \int_{\Gamma^{Fe}} \left[w \left(\left(\rho_f C_{pF} \right)_{\text{eff}} - S_{gF} R \sum_{j=1}^{n_g} c_f^j \right) N_F^T \mathbf{R}^T \mathbf{R} N_F \right] d\Gamma^{Fe}$$

$$\mathbf{C}_{ul, m} = \sum_{e=1}^{n_{ele}} \int_{\Omega^e} \mathbf{P} [\mathbf{I} \alpha_m S_{lm}] N d\Omega^e$$

$$\mathbf{C}_{ul, f} = \sum_{e=1}^{n_{ele}} \int_{\Omega^e} \mathbf{P} [\mathbf{I} \alpha_f S_{lf}] N d\Omega^e$$

$$\mathbf{C}_{ue_{gm}^i} = \sum_{e=1}^{n_{ele}} \int_{\Omega^e} \mathbf{P} \left[\mathbf{I} \alpha_m S_{gm} Z_m R T_m - \frac{1}{3} \mathbf{D} \mathbf{I} A_s^i \right] N d\Omega^e$$

$$\mathbf{C}_{ue_{gf}^i} = \sum_{e=1}^{n_{ele}} \int_{\Omega^e} \mathbf{P} [\mathbf{I} \alpha_f S_{gf} Z_f R T_f] N d\Omega^e$$

$$\mathbf{C}_{uT_m} = \sum_{e=1}^{n_{ele}} \mathbf{P} \left[\mathbf{I} \alpha_m S_{gm} Z_m R \sum_{j=1}^{n_g} c_m^j - \frac{1}{3} \mathbf{D} \mathbf{I} A_T \right] N d\Omega^e$$

$$\mathbf{C}_{uT_f} = \sum_{e=1}^{n_{ele}} \mathbf{P} \left[\mathbf{I} \alpha_f S_{gf} Z_f R \sum_{j=1}^{n_g} c_{gf}^j \right] N d\Omega^e$$

$$\mathbf{C}_{uu} = \sum_{e=1}^{n_{ele}} \int_{\Omega^e} [\mathbf{P} \mathbf{D} \mathbf{P}^T] d\Omega^e$$

$$\mathbf{K}_{ll, m} = \sum_{e=1}^{n_{ele}} \int_{\Omega^e} \left[\frac{K_{rlm} K_m}{\mu_m} \nabla N^T \nabla N + \sigma_l N^T N \right] d\Omega^e$$

$$\mathbf{K}_{ll, mf} = \sum_{e=1}^{n_{ele}} \int_{\Omega^e} [-\sigma_l N^T N] d\Omega^e$$

$$\mathbf{K}_{ll, f+F} = \sum_{e=1}^{n_{ele}} \int_{\Omega^e} \left[\frac{K_{rlf} K_f}{\mu_f} \nabla N^T \nabla N + \sigma_l N^T N \right] d\Omega^e + \sum_{e=1}^{n_{eleF}} \int_{\Gamma^{Fe}} \left[\frac{K_{rlF} W^3}{12 \mu_f} \nabla_l N_F^T \mathbf{R}^T \mathbf{R} \nabla_l N_F \right] d\Gamma^{Fe}$$

$$\mathbf{K}_{ll, fm} = \sum_{e=1}^{n_{ele}} \int_{\Omega^e} [-\sigma_l N^T N] d\Omega^e$$

$$\mathbf{K}_{c_g^i, l, m} = \sum_{e=1}^{n_{ele}} \int_{\Omega^e} [\bar{c}_d \sigma_l N^T N] d\Omega^e$$

$$\mathbf{K}_{c_g^i, l, mf} = \sum_{e=1}^{n_{ele}} \int_{\Omega^e} [-\bar{c}_d \sigma_l N^T N] d\Omega^e$$

$$\mathbf{K}_{c_g^i, c_g^j, m} = \sum_{e=1}^{n_{ele}} \int_{\Omega^e} \left[\left(c_{gm}^i \frac{K_m K_{rgm}}{\mu_g} Z_m T_m R + S_{gm} D_{gem} \delta_{ij} + S_{lm} D_{dem} H_g^i \delta_{ij} \right) \nabla N^T \nabla N \right] d\Omega^e$$

$$\mathbf{K}_{c_g^i, T, m} = \sum_{e=1}^{n_{ele}} \int_{\Omega^e} \left[c_{gm}^i \frac{K_m K_{rgm}}{\mu_g} Z_m T_m R \nabla N^T \nabla N \right] d\Omega^e$$

$$\mathbf{K}_{c_g^i, l, f} = \sum_{e=1}^{n_{ele}} \int_{\Omega^e} [\bar{c}_d \sigma_l N^T N] d\Omega^e$$

$$\mathbf{K}_{c_g^i, l, fm} = \sum_{e=1}^{n_{ele}} \int_{\Omega^e} [-\bar{c}_d \sigma_l N^T N] d\Omega^e$$

$$\mathbf{K}_{c_g^i, c_g^j, f+F} = \sum_{e=1}^{n_{ele}} \int_{\Omega^e} \left[\left(c_{gf}^i \frac{K_f K_{rgf}}{\mu_g} Z_f T_f R \right) \nabla N^T \nabla N \right] d\Omega^e + \sum_{e=1}^{n_{eleF}} \int_{\Gamma^{Fe}} \left[c_{fF}^i \frac{K_{rF} W^3}{12 \mu_{gF}} Z_f R T_f \nabla_l N_F^T \mathbf{R}^T \mathbf{R} \nabla_l N_F \right] d\Gamma^{Fe}$$

$$\mathbf{K}_{\text{gT},f+F}^{\text{K}} = \sum_{e=1}^{n_{\text{ele}}} \int_{\Omega^e} \left[\left(c_{\text{gf}}^i \frac{K_f K_{\text{rgf}}}{\mu_g} Z_f R \sum_{j=1}^{n_g} c_{\text{gf}}^j + S_{\text{gf}} D_{\text{gef}} \delta_{ij} + S_{\text{yf}} D_{\text{def}} H_g^i \delta_{ij} \right) \nabla N^T \nabla N \right] d\Omega^e + \sum_{e=1}^{n_{\text{eleF}}} \int_{\Gamma^{Fe}} \left[\frac{K_{\text{rgf}} W^3}{12 \mu_{\text{gf}}} Z_f R \sum_{j=1}^{n_g} c_{\text{gf}}^j \nabla_t N_F^T \mathbf{R}^T \mathbf{R} \nabla_t N_F \right] d\Gamma^{Fe}$$

$$\mathbf{K}_{\text{TT},m} = \sum_{e=1}^{n_{\text{ele}}} \int_{\Omega^e} [\lambda_{em} \nabla N^T \nabla N] d\Omega^e$$

$$\mathbf{K}_{\text{TT},f+F} = \sum_{e=1}^{n_{\text{ele}}} \int_{\Omega^e} [\lambda_{\text{ef}} \nabla N^T \nabla N] d\Omega^e + \sum_{e=1}^{n_{\text{eleF}}} \int_{\Gamma^{Fe}} [w \lambda_{\text{ef}} N_F^T \mathbf{R}^T \mathbf{R} \nabla N_F] d\Gamma^{Fe}$$

$$\mathbf{K}_{\text{TT},f+F}^{\text{V}} = \sum_{e=1}^{n_{\text{ele}}} \int_{\Omega^e} [(-S_{\text{gf}} \rho_{\text{gf}} C_{\text{pgf}} \mathbf{v}_{\text{gf}} - S_{\text{yf}} \rho_l C_{\text{pl}} \mathbf{v}_{\text{yf}}) N^T \nabla N] d\Omega^e + \sum_{e=1}^{n_{\text{eleF}}} \int_{\Gamma^{Fe}} [(-w S_{\text{gf}} \rho_{\text{gf}} C_{\text{pgf}} \mathbf{v}_{\text{gf}} - w S_{\text{lf}} \rho_l C_{\text{pl}} \mathbf{v}_{\text{lf}}) N_F^T \mathbf{R}^T \mathbf{R} \nabla N_F] d\Gamma^{Fe}$$

$$\mathbf{f}_{\text{im}} = \sum_{e=1}^{n_{\text{ele}}} \int_{\Gamma^e} N_s^T [f_{\text{i,m}}] \underline{n} d\Gamma^e$$

$$\mathbf{f}_{\text{if}} = \sum_{e=1}^{n_{\text{ele}}} \int_{\Gamma^e} N_s^T [f_{\text{i,f}}] \underline{n} d\Gamma^e$$

$$\mathbf{f}_{\text{gm}}^{\text{i}} = \sum_{e=1}^{n_{\text{ele}}} \int_{\Gamma^e} N^T [f_{\text{g,m}}^j] \underline{n} d\Gamma^e$$

$$\mathbf{f}_{\text{gf}}^{\text{i}} = \sum_{e=1}^{n_{\text{ele}}} \int_{\Gamma^e} N^T [f_{\text{g,f}}^j] \underline{n} d\Gamma^e$$

$$\mathbf{f}_{\text{Tm}} = \sum_{e=1}^{n_{\text{ele}}} \int_{\Gamma^e} N^T [f_{\text{T,m}}] \underline{n} d\Gamma^e$$

$$\mathbf{f}_{\text{Tf}} = \sum_{e=1}^{n_{\text{ele}}} \int_{\Gamma^e} N^T [f_{\text{T,f}}] \underline{n} d\Gamma^e$$

$$\mathbf{f}_{\text{u}} = \sum_{e=1}^{n_{\text{ele}}} \int_{\Gamma^e} [N \widehat{\mathbf{T}}_r] d\Gamma^e$$

References

- Barenblatt, G., Zheltov, I.P., Kochina, I., 1960. Basic concepts in the theory of seepage of homogeneous liquids in fissured rocks [strata]. *J. Appl. Math. Mech.* 24, 1286–1303.
- Bogdanov, I., Mourzenko, V., Thovert, J.-F., Adler, P., 2003. Two-phase flow through fractured porous media. *Phys. Rev. E* 68, 026703.
- Castro, H.G., Paz, R.R., Storti, M.A., Sonzogni, V.E., Dalcín, L., 2009. Parallel Implementation of a FEM code by using MPI/PETSC and OPENMP hybrid programming techniques. *Mecánica Computacional* 28, 205–215.
- Chen, M., 2019. Modelling of Gas Transport in Coal-a Hybrid Coupled Dual Porosity and Discrete Fracture Approach.
- Chen, M., Hosking, L.J., Sandford, R.J., Thomas, H.R., 2019. Dual porosity modelling of the coupled mechanical response of coal to gas flow and adsorption. *Int. J. Coal Geol.* 205, 115–125.
- Chen, M., Hosking, L.J., Sandford, R.J., Thomas, H.R., 2020a. A coupled compressible flow and geomechanics model for dynamic fracture aperture during carbon sequestration in coal. *Int. J. Numer. Anal. Methods Geomech.* 44 (13), 1727–1749.
- Chen, M., Hosking, L.J., Sandford, R.J., Thomas, H.R., 2020b. Numerical Analysis of Improvements to CO₂ Injectivity in Coal Seams through Stimulated Fracture connection to the Injection well. *Rock Mech. Rock. Eng.* 1–20.
- Chen, M., Masum, S., Thomas, H., 2020c. Modeling Non-isothermal Transport Behavior of Real Gas in Deformable Coal Matrix. *Energy Fuel* 35, 1605–1619.
- Chen, M., Masum, S., Thomas, H., 2021. Modeling adsorption and transport behavior of gases in moist coal matrix. *Energy Fuel* 35, 13200–13214.
- Chen, M., Masum, S., Sadasivam, S., Thomas, H., 2022. Modelling anisotropic adsorption-induced coal swelling and stress-dependent anisotropic permeability. *Int. J. Rock Mech. Min. Sci.* 153, 105107.
- Chiang, K., Fulton, R., 1990. Concepts and implementation of parallel finite element analysis. *Comput. Struct.* 36, 1039–1046.
- Chung, T.H., Ajan, M., Lee, L.L., Starling, K.E., 1988. Generalized multiparameter correlation for nonpolar and polar fluid transport properties. *Ind. Eng. Chem. Res.* 27, 671–679.
- Cui, L.-Y., Masum, S.A., Ye, W.-M., Thomas, H.R., 2022. Investigation on gas migration behaviours in saturated compacted bentonite under rigid boundary conditions. *Acta Geotech.* 17, 2517–2531.
- Geist, A., Beguelin, A., Dongarra, J., Jiang, W., Manchek, R., Sunderam, V.S., 1994. PVM: Parallel Virtual Machine: A users' Guide and Tutorial for Networked Parallel Computing. MIT press.
- Gerke, H., Genuchten, M.v., 1993. Evaluation of a first-order water transfer term for variably saturated dual-porosity flow models. *Water Resour. Res.* 29, 1225–1238.
- Gupta, S., Helmig, R., Wohlmuth, B., 2015. Non-isothermal, multi-phase, multi-component flows through deformable methane hydrate reservoirs. *Comput. Geosci.* 19, 1063–1088.
- Hao, Y., Fu, P., Carrigan, C.R., 2013. Application of a dual-continuum model for simulation of fluid flow and heat transfer in fractured geothermal reservoirs. *Proceedings. In: 38th Workshop on Geothermal Reservoir Engineering, Vol SGP-TR-198. Stanford University, Stanford, California, pp. 462–469.*
- Heinze, T., Hamidi, S., 2017. Heat transfer and parameterization in local thermal non-equilibrium for dual porosity continua. *Appl. Therm. Eng.* 114, 645–652.
- Hosking, L.J., Thomas, H.R., Sedighi, M., 2017. A dual porosity model of high-pressure gas flow for geoenery applications. *Can. Geotech. J.* 55, 839–851.
- Hosking, L.J., Chen, M., Thomas, H.R., 2020. Numerical analysis of dual porosity coupled thermo-hydro-mechanical behaviour during CO₂ sequestration in coal. *Int. J. Rock Mech. Min. Sci.* 135, 104473.
- Jenabidehkordi, A., 2019. Computational methods for fracture in rock: a review and recent advances. *Front. Struct. Civ. Eng.* 13, 273–287.
- Jimack, P., Touheed, N., 2000. Developing parallel finite element software using MPI. *In: High Performance Computing for Computational Mechanics, pp. 15–38.*
- Jing, L., 2003. A review of techniques, advances and outstanding issues in numerical modelling for rock mechanics and rock engineering. *Int. J. Rock Mech. Min. Sci.* 40, 283–353.
- Karypis, G., Kumar, V., 1999. Parallel multilevel series k-way partitioning scheme for irregular graphs. *SIAM Rev.* 41, 278–300.
- Kolditz, O., Adamidis, P., Bauer, S., Du, Y., Hess, M., Kemmler, D., Kosakowski, G., McDermott, C., Wang, W., Rabenseifner, R., 2006. High Performance Computing in Applied Geosciences.
- Kühne, R., Ebert, R.-U., Schürmann, G., 2005. Prediction of the temperature dependency of Henry's law constant from chemical structure. *Environ. Sci. Technol.* 39, 6705–6711.
- Lanucara, P., Rovida, S., 1999. Conjugate-Gradient Algorithms: an MPI Open-MP Implementation on distributed Shared memory Systems, First European Workshop on OpenMP. *In: Citeseer, pp. 76–78.*

- Lei, Q., Latham, J.-P., Tsang, C.-F., 2017. The use of discrete fracture networks for modelling coupled geomechanical and hydrological behaviour of fractured rocks. *Comput. Geotech.* 85, 151–176.
- Lewis, R., Pao, W., 2002. Numerical simulation of three-phase flow in deforming fractured reservoirs. *Oil Gas Sci. Technol.* 57, 499–514.
- Lewis, R., Schrefler, B., 1998. The finite element method in the static and dynamic deformation and consolidation of porous media. John Wiley & Sons, Chichester, UK. In: *The finite element method in the static and dynamic deformation and consolidation of porous media*, 2nd ed. John Wiley & Sons, Chichester, UK.
- Ma, T., Rutqvist, J., Oldenburg, C.M., Liu, W., 2017. Coupled thermal–hydrological–mechanical modeling of CO₂-enhanced coalbed methane recovery. *Int. J. Coal Geol.* 179, 81–91.
- Mahinthakumar, G., Saied, F., 2002. A hybrid MPI-OpenMP implementation of an implicit finite-element code on parallel architectures. *The. Int. J. High Perform. Comput. Appl.* 16, 371–393.
- Masum, S.A., Chen, M., Hosking, L.J., Stanczyk, K., Kapusta, K., Thomas, H.R., 2022. A numerical modelling study to support design of an in-situ CO₂ injection test facility using horizontal injection well in a shallow-depth coal seam. *Int. J. Greenhouse Gas Control* 119, 103725.
- Moinfar, A., Varavei, A., Sepehrmoori, K., Johns, R.T., 2013. Development of a coupled dual continuum and discrete fracture model for the simulation of unconventional reservoirs, SPE reservoir simulation symposium. In: *Society of Petroleum Engineers*.
- Nieplocha, J., Ju, J., 2000. ARMC: a portable aggregate remote memory copy interface. In: *Citeseer*.
- Nikoosokhan, S., Brochard, L., Vandamme, M., Dangla, P., Pellenq, R.J.M., Lecampion, B., Fen-Chong, T., 2012. CO₂ Storage in Coal Seams. In: *Coupling Surface Adsorption and Strain. Geomechanics in CO₂ Storage Facilities*, pp. 115–132.
- Nikoosokhan, S., Brochard, L., Vandamme, M., Dangla, P., Pellenq, R.J.M., Lecampion, B., Fen-Chong, T., 2013. CO₂ Storage in Coal Seams: Coupling Surface Adsorption and Strain, pp. 115–132.
- Pacheco, P., 2011. *An Introduction to Parallel Programming*. Elsevier.
- Pao, W.K., Lewis, R.W., 2002. Three-dimensional finite element simulation of three-phase flow in a deforming fissured reservoir. *Comput. Methods Appl. Mech. Eng.* 191, 2631–2659.
- Peng, D.-Y., Robinson, D.B., 1976. A new two-constant equation of state. *Ind. Eng. Chem. Fundam.* 15, 59–64.
- Pini, R., Ottiger, S., Burlini, L., Storti, G., Mazzotti, M., 2009. Role of adsorption and swelling on the dynamics of gas injection in coal. *J. Geophys. Res. Solid Earth* 114.
- Pouya, A., 2015. A finite element method for modeling coupled flow and deformation in porous fractured media. *Int. J. Numer. Anal. Methods Geomech.* 39, 1836–1852.
- Rutqvist, J., Wu, Y.-S., Tsang, C.-F., Bodvarsson, G., 2002. A modeling approach for analysis of coupled multiphase fluid flow, heat transfer, and deformation in fractured porous rock. *Int. J. Rock Mech. Min. Sci.* 39, 429–442.
- Sass, J., Lachenbruch, A.H., Munroe, R.J., 1971. Thermal conductivity of rocks from measurements on fragments and its application to heat-flow determinations. *J. Geophys. Res.* 76, 3391–3401.
- Smith, I.M., Griffiths, D.V., Margetts, L., 2013. *Programming the Finite Element Method*. John Wiley & Sons.
- Smith, L., Bull, M., 2001. Development of mixed mode MPI/OpenMP applications. *Sci. Program.* 9, 83–98.
- Strack, O.D., 1982. Assessment of Effectiveness of Geologic Isolation Systems. Analytic modeling of flow in a permeable fissured medium, Pacific Northwest Lab.
- Su, D., Mayer, K.U., MacQuarrie, K.T., 2017. Parallelization of MIN3P-THCm: a high performance computational framework for subsurface flow and reactive transport simulation. *Environ. Model. Softw.* 95, 271–289.
- Taron, J., Elsworth, D., Min, K.-B., 2009. Numerical simulation of thermal-hydrologic-mechanical-chemical processes in deformable, fractured porous media. *Int. J. Rock Mech. Min. Sci.* 46, 842–854.
- Thomas, H., He, Y., 1997. A coupled heat–moisture transfer theory for deformable unsaturated soil and its algorithmic implementation. *Int. J. Numer. Methods Eng.* 40, 3421–3441.
- Thomas, H.R., He, Y., 1998. Modelling the behaviour of unsaturated soil using an elastoplastic constitutive model. *Géotechnique* 48, 589–603.
- Thomas, H.R., Vardon, P.J., Li, Y.-C., 2010. Coupled thermo-hydro-chemo-mechanical modeling for geoenvironmental phenomena. In: *Advances in Environmental Geotechnics*. Springer, pp. 320–327.
- Van der Vorst, H.A., 1992. Bi-CGSTAB: a fast and smoothly converging variant of Bi-CG for the solution of nonsymmetric linear systems. *SIAM J. Sci. Stat. Comput.* 13, 631–644.
- Van Genuchten, M.T., 1980. A closed-form equation for predicting the hydraulic conductivity of unsaturated soils 1. *Soil Sci. Soc. Am. J.* 44, 892–898.
- Vardon, P.J., Banicescu, I., Cleall, P.J., Thomas, H.R., Philp, R.N., 2009. Coupled thermo-hydro-mechanical modelling: a new parallel approach, 2009 IEEE International Symposium on parallel & distributed Processing. *IEEE* 1–9.
- Vardon, P.J., Cleall, P.J., Thomas, H.R., Philp, R.N., Banicescu, I., 2011. Three-dimensional field-scale coupled thermo-hydro-mechanical modeling: parallel computing implementation. *Int. J. Geomech.* 11, 90–98.
- Walker, D.W., Dongarra, J.J., 1996. MPI: a standard message passing interface. *Supercomputer* 12, 56–68.
- Wang, M., Hosking, L., Masum, S., Thomas, H., 2016. Development of a High Performance Computing Approach for Studying the Coupled Behaviour of Porous Media.
- Wang, W., Kosakowski, G., Kolditz, O., 2009. A parallel finite element scheme for thermo-hydro-mechanical (THM) coupled problems in porous media. *Comput. Geosci.* 35, 1631–1641.
- Wang, W., Kolditz, O., Nagel, T., 2017. Parallel finite element modelling of multi-physical processes in thermochemical energy storage devices. *Appl. Energy* 185, 1954–1964.
- Warren, J., Root, P.J., 1963. The behavior of naturally fractured reservoirs. *Soc. Pet. Eng. J.* 3, 245–255.
- Zienkiewicz, O.C., Taylor, R.L., Zhu, J.Z., 2005. *The Finite Element Method: Its Basis and Fundamentals*. Elsevier.